

THESIS FOR THE DEGREE OF DOCTOR OF PHILOSOPHY

Structure-dynamics relationships in perovskite oxyhydrides and alkali silanides

CARIN EKLÖF-ÖSTERBERG



CHALMERS

Department of Chemistry and Chemical Engineering

CHALMERS UNIVERSITY OF TECHNOLOGY

Gothenburg, Sweden 2019

**Structure-dynamics relationships in perovskite oxyhydrides and
alkali silanides**

CARIN EKLÖF-ÖSTERBERG

ISBN 978-91-7597-845-1

© CARIN EKLÖF-ÖSTERBERG, 2019

Doktorsavhandlingar vid Chalmers tekniska högskola

Ny serie nr 4526

ISSN 0346-718X

Department of Chemistry and Chemical Engineering

Chalmers University of Technology

SE-412 96 Göteborg

Sweden

Telephone: +46(0)31-722 1000

Cover: Artistic interpretation of the hydride ion dynamics in perovskite oxyhydride and the localised diffusion of the silanide ion.

Printed by Chalmers Reproservice AB

Göteborg, Sweden 2019

Structure-dynamics relationships in perovskite oxyhydrides and alkali silanides

Carin Eklöf-Österberg
Department of Chemistry and Chemical Engineering
Chalmers University of Technology

Abstract

This thesis focuses on investigations of the local structure and dynamics of two classes of hydrogen-containing, energy relevant, materials; perovskite type oxyhydrides $\text{BaTiO}_{3-x}\text{H}_x$ and alkali silanides ASiH_3 ($A = \text{K}$ and Rb). In the area of oxyhydrides, which are of relevance for the development of electrolytes in fuel cells and batteries, the aim is to elucidate the dynamics and electronic character of the hydrogen species in the materials. This is of great importance for developing new efficient synthesis routes and novel applications for oxyhydrides. The main tools of choice for these investigations are quasielastic and inelastic neutron scattering (QENS and INS, respectively). The results show that the hydride ion exhibits a long-range diffusion with a jump length corresponding to nearest neighbour (NN) jumps at low temperatures (225–250 K) and second nearest neighbour (2NN) jumps at high temperatures (400–700 K). Importantly, the hydride-ion diffusivity was shown to be mediated by oxygen vacancies present in the material. Furthermore, the results from INS combined with density functional theory calculations show that the extra electron, originating from the hydride ion, forms a delocalised bandstate, as opposed to a localised polaronic state as suggested elsewhere.

In the area of alkali silanides, which are of interest as hydrogen storage materials, the aim was to investigate the origin of the low entropy variation that these materials exhibit during the absorption/desorption process, using QENS. The results point towards complex dynamics, characterised by a quasi-spherical localised jump diffusion with 24 different preferred sites at high temperatures and slower C_3 axis rotations as the dynamical motions starts to "freeze in" closer to the phase transition at lower temperatures. Specifically, at high temperatures the SiH_3^- ions are almost freely rotating, similar to how the ions behaves in a gas, which explains the origin of the low entropy variation and should be something to strive for when developing new hydrogen storage materials.

Keywords: *hydride ion conduction, hydrogen storage material, hydrogen dynamics, localized motion, long range diffusion, oxyhydride, neutron scattering*

The thesis reflects the content of the following appended papers

I Dynamics of hydride ions in metal hydride-reduced BaTiO_3 samples investigated with quasielastic neutron scattering

Carin Eklöf-Österberg, Reji Nedumkandathil, Ulrich Häussermann, Aleksander Jaworski, Andrew J. Pell, Madhusudan Tyagi, Niina H. Jalarvo, Bernhard Frick, Antonio Faraone, Maths Karlsson
Journal of Physical Chemistry C **123**, 2019-2030 (2019)

II Band vs polaron: vibrational motion and chemical expansion of hydride ions as signatures for the electronic character in oxyhydride barium titanate

Erik Jedvik Granhed, Anders Lindman, Carin Eklöf-Österberg, Maths Karlsson, Stewart F. Parker and Göran Wahnström
Submitted

III Local structure and vibrational dynamics of metal hydride reduced BaTiO_3

Carin Eklöf-Österberg, Laura Mazzei, Erik Jedvik Granhed, Göran Wahnström, Reji Nedumkandathil, Ulrich Häussermann, Stewart F. Parker, Niina H. Jalarvo, Lars Börjesson, Maths Karlsson
In manuscript

IV Vacancy mediated water intercalation into Rhenium trioxide and the influence of each on negative thermal expansion properties and thermal stability

Paul F. Henry, Carin Eklöf-Österberg, Thomas C. Hansen, Emmanuelle Suard, Mark T. Weller, Maths Karlsson
In manuscript

V Dynamics of Pyramidal SiH_3^- Ions in ASiH_3 ($A = \text{K}$ and Rb) Investigated with Quasielastic Neutron Scattering

Carin Österberg, Henrik Fahlquist, Ulrich Häussermann, Craig M. Brown, Terrence J. Udovic, Maths Karlsson
Journal of Physical Chemistry C **120**, 6369-6376 (2016)

**VI Investigation of the Order-Disorder Rotator Phase Transition in
KSiH₃ and RbSiH₃**

Reji Nedumkandathil, Aleksander Jaworski, Andreas Fischer, Carin Österberg, Yuan-Chih Lin, Maths Karlsson, Jekabs Grins, Andrew J. Pell, Matthias Eden, Ulrich Häussermann

Journal of Physical Chemistry C **121**, 5241-5252 (2017)

My contributions to the appended papers

- I The author did the QENS experiments, the analysis of the QENS data, wrote the first draft and was the main author of the paper.
- II The author did the INS experiments, the analysis of the INS data, wrote the experimental part of the paper and participated in the discussion about the results.
- III The author did the INS experiments. The analysis of the INS data, and the writing of the first draft of the paper, were done together with Laura Mazzei.
- IV The author did the diffraction experiment and analysis in close collaboration with Paul Henry. The author wrote the first draft.
- V The author did the QENS experiments, the data analysis, wrote the first draft and was the main author of the paper.
- VI The author did the QENS experiments, the analysis of the QENS data, wrote the corresponding sections in the paper and participated in the discussion about the results.

Other publications to which I have contributed to during my PhD studies, but that are not part of the thesis.

Hydride Reduction of BaTiO₃ Oxyhydride Versus O-Vacancy Formation

Reji Nedumkandathil, Aleksander Jaworski, Jekabs Grins, Diana Bernin, Maths Karlsson, Carin Eklöf-Österberg, Alexandra Neagu, Cheuk-wai Tai, Andrew J. Pell, and Ulrich Häussermann
ACS Omega **3**, 11426-11438 (2018)

Vibrational properties of β -KSiH₃ and β -RbSiH₃: a combined Raman and inelastic neutron scattering study

Janos Mink, Yuan-Chih Lin, Maths Karlsson, Carin Österberg, Terrence J. Udovic, Henrik Fahlquist and Ulrich Häussermann
Journal of Raman Spectroscopy **48**, 284-291 (2017)

Contents

1	Introduction	1
2	Hydride structure and dynamics in solid state materials	7
2.1	General aspects of hydrides	7
2.2	Transition metal oxyhydrides	8
2.2.1	Topochemical reaction synthesis	9
2.2.2	Perovskite type oxyhydride $ATiO_{3-x}H_x$	10
2.3	Metal and complex hydrides	19
2.3.1	Metal hydrides	19
2.3.2	Complex hydrides	21
2.3.3	The $ASiH_3$ material	24
3	Methodology	27
3.1	General aspects of neutron scattering	27
3.2	Neutron diffraction	29
3.3	Inelastic neutron scattering	31
3.3.1	Mean-square displacement	32
3.4	Quasielastic neutron scattering	35
3.4.1	Elastic incoherent structure factor	37
3.5	Neutron Spin-Echo	40
4	Instrumentation	41
4.1	Neutron sources and the production of neutrons	41
4.2	Inelastic spectrometers	42
4.3	Quasielastic spectrometers	43
4.3.1	The Disc Chopper Spectrometer	43

4.3.2	Backscattering spectrometers	44
4.3.3	Neutron spin-echo	46
4.4	Neutron diffractometer	46
5	Results	49
5.1	Local structure and dynamics of perovskite type oxyhydrides . .	49
5.2	Localised hydrogen diffusion in alkali silanides	55
6	Conclusions and outlook	61
A	Inelastic neutron scattering details	65
A.1	MSD derived from the Q -dependence	65
B	Neutron spin-echo details	69
B.1	Operation principle	69
	Acknowledgments	71
	Bibliography	73
	Papers I-VI	90

Glossary

DCS	Disk Chopper Spectrometer
DFT	Density Functional Theory
DOE	US Department Of Energy
EISF	Elastic Incoherent Structure Factor
ESS	European Spallation Source
FT	Fourier Transform
FWHM	Full Width at Half Maximum
EFWS	Elastic Fixed Window Scan
HFBS	High Flux Backscattering Spectrometer
ILL	Institut Laue-Langevin
INS	Inelastic Neutron Scattering
MSD	Mean-Square Displacement
NIST	National Institute of Standards and Technology
NCNR	NIST Center for Neutron Research
NPD	Neutron Powder Diffraction
NSE	Neutron Spin-Echo
NTE	Negative Thermal Expansion
P-T window	Pressure-Temperature window
PEM	Polymer Electrolyte Membranes
QENS	Quasielastic neutron scattering
RT	Room Temperature
SNS	Spallation Neutron Source
TGA	Thermal Gravimetric Analysis

1

Introduction

Currently there is a worldwide goal to reduce the carbon dioxide (CO_2) emissions in order to avoid a yearly average global temperature increase of $2\text{ }^\circ\text{C}$ from that of the pre-industrial times [1, 2]. Therefore, alternatives of how to harvest energy need to be implemented, that is to instead use energy sources that are naturally replenished on a human timescale, so called renewable energy [3], need to be developed. This include energy sources such as wind-, wave- or solar-energies, but the famous issue is to get an even energy distribution also when the wind is not blowing, when the ocean is calm and when the sun is not shining [4–6]. It is therefore important to consider how to store the renewable energy in an efficient way. An alternative is to store the energy chemically as hydrogen gas (H_2), either chemically bound as in a solid or mechanically as in a pressurised gas [7, 8] [Fig. 1.1(a)]. Research of various aspects of hydrogen in matter is therefore becoming increasingly important [9–12].

In particular, there is a large effort devoted to the development of materials that can either store or conduct hydrogen, or both, which can be used in, or in connection to, so called hydrogen fuel cells[Fig. 1.1(b)]. These are devices that in a combination with efficient and functional storage of hydrogen are one of the most promising, yet challenging, solutions for the creation of a more environmentally friendly and sustainable future. In particular, the use of so-called intermediate temperature ($200\text{--}500\text{ }^\circ\text{C}$) fuel cell technology, would in many cases advance the application sphere of fuel cells due to its ability to provide; short start-up times, the possibility to use different types of fuels,

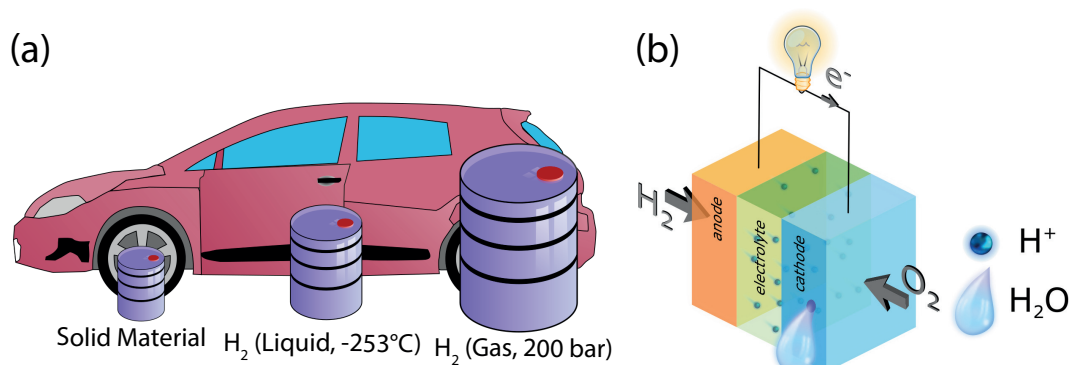


Figure 1.1: (a) Schematic illustration of the volume of 4 kg of hydrogen (≈ 400 km driving range) in different storage media [23, 24] and (b) a hydrogen fuel cell.

advantageous in terms of long-term operation, materials stability and lower costs [13–15].

One of the most crucial requirements for the efficient operation of fuel cells is a good conductivity of the electrolyte, *i.e.* in the material that provides transport of ions (*e.g.* H^+) between the two electrodes (anode and cathode), see Fig. 1.1(b). However, for the intermediate temperature range it has been difficult to develop such materials [13–16]. In this context, many acceptor-doped perovskite structured oxides, *i.e.* $A_{1-x}A'_x B_{1-y}B'_y \text{O}_{3+/-\delta}$ (where A = a cation of larger size, A' = partial substitution of cations in positions A , B = a cation of smaller size and B' = partial substitution of cations in positions B , O = oxygen with either more, $+\delta$, or less, $-\delta$, occupancy than the original perovskite structure of ABO_3) [17], exhibit a good chemical and mechanical stability combined with high levels of proton conductivity [18, 19]. However, compared to polymer electrolyte membranes (PEMs), which is the electrolyte currently used in the much more established low-temperature (< 100 °C) fuel cells, the conductivity in perovskite type oxides is still too low for most technological applications [4, 20–22]. In order to identify new materials with a higher conductivity than those already available and which thus can allow intermediate temperature fuel cells to be developed, one needs to advance the current knowledge about how hydrogen moves (*i.e.* dynamics) in solids.

One opportunity to advance our understanding of hydrogen (or proton) transport in perovskite structured materials is given by the recently discovered

perovskite type oxyhydrides. These materials show many interesting features, which have several important applications, such as mixed anionic/electronic conductivity that may be utilised for electrode materials [Fig. 1.2(d)] [25–30], as convenient precursors for reactions and compounds [31], and even as high-potential electrochemical cells based on the H^-/H^+ oxidation-reduction (redox) couple [32][Fig. 1.2(e)]. However, these are novel materials and much about their structure and dynamics is not fully understood. For example, it is vital to investigate how the dynamics of the hydrogen species are influenced by its surrounding structure and, contrary, how the local environment behaves by the influence of the hydride ions. Such fundamental knowledge would not only pave the way for further development of perovskite oxyhydrides but would certainly expand our knowledge about hydrogen transport in materials more generally. This can, *e.g.* be expected to be important for the development of new, highly proton conducting materials based on the perovskite structure or similar structure types. Additionally, knowledge about hydride ion conduction through an oxide material may as well advance our understanding of how to develop new anion conductors, such as oxide-, fluoride-, chloride- and iodide-ion conductors [16, 33–37], *i.e.* not limited to hydrogen species.

Apart from a high proton conductivity of the fuel cell electrolyte, an efficient and functional storage of the fuel (H_2) is equally important for the utilisation of fuel cells in technological applications. The US department of energy (DOE) claims that a desorption temperature of 60–120 °C and a storage density of 6.5 weight percent (wt.%) will be required for fuel cell powered vehicles in order to meet customer performance expectations for driving range, passengers and cargo space, refuelling time, and overall vehicle performance [38]. A specific challenge is to store the hydrogen in a safe (hydrogen gas is explosive), efficient and economical way [23, 39]. There are primarily three ways to store hydrogen; as a gas, a liquid, or as a solid [Fig. 1.1(a)]. If one chooses to store the hydrogen as a gas [40], the pressurising and depressurising of the gas needs to be dealt with as the work pressure for a hydrogen-based device lies close to ambient pressure. If one chooses to store the hydrogen as a liquid, the temperature is a factor that needs to be considered, due to the fact that hydrogen gas becomes liquid at 20 K [41]. That leaves us with the, often favourable, alternative of a solid hydrogen storage. The specific demands on such a material is that the

hydrogen exchange must take place under mild pressures (close to atmospheric pressure) [42, 43] and at temperatures close to room temperature (RT) [42, 43], in order to connect well with the rest of the fuel cell system. To meet these demands one approach is to develop a metal hydride or complex hydride material exhibiting both quick absorption/desorption and a high density of hydrogen atoms in the fully hydrogenated material [44]. However, present day metal hydride and complex hydride materials for hydrogen storage are featured by a too low hydrogen storage capacity and/or slow absorption kinetics [8, 45, 46]. The development of new better materials depends on a thorough understanding of the behaviour of hydrogen, and how it relates to the details of the crystal structure, in metal hydride and complex hydride materials. However, for many materials the hydrogen dynamics are rather unexplored and therefore in which way the hydrogen dynamics correlate to hydrogen storage characteristics is still not fully understood [47, 48].

Alkali silanides show many highly important characteristics for hydrogen storage purposes; that is the reversibility of H_2 absorption with up to 4.3 wt.% possible exchange within a good pressure and temperature window at 0.1 MPa hydrogen equilibrium pressure at 414 K [44, 47]. However, the physicochemical reasons involved in the hydrogen exchange process remain unknown. This makes the alkali silanides a highly interesting and important material to study in order to further develop our understanding of what material characteristics that are needed in order to develop new, highly efficient, hydrogen storage materials. This then boils down to a pure question of material design, to either improve present-day materials or to explore possible new systems [40, 49–51]. An especially important challenge is to uncover the, relatively unknown, mechanistic aspects (*i.e.* the time-scale, activation energy, and spatial geometry) of the hydrogen diffusion process.

In order to take on some of these materials science challenges, this thesis, which is mainly experimental in nature, deals with detailed studies of the structure-dynamics-property relations in two classes of hydrogen containing, energy relevant, materials; *perovskite type oxyhydrides* and *alkali silanides*. The aim of the thesis is to develop new understanding pertaining to structure-dynamics-property relationships in these two classes of materials and, on the basis of this new knowledge, discuss how to design new and more efficient "en-

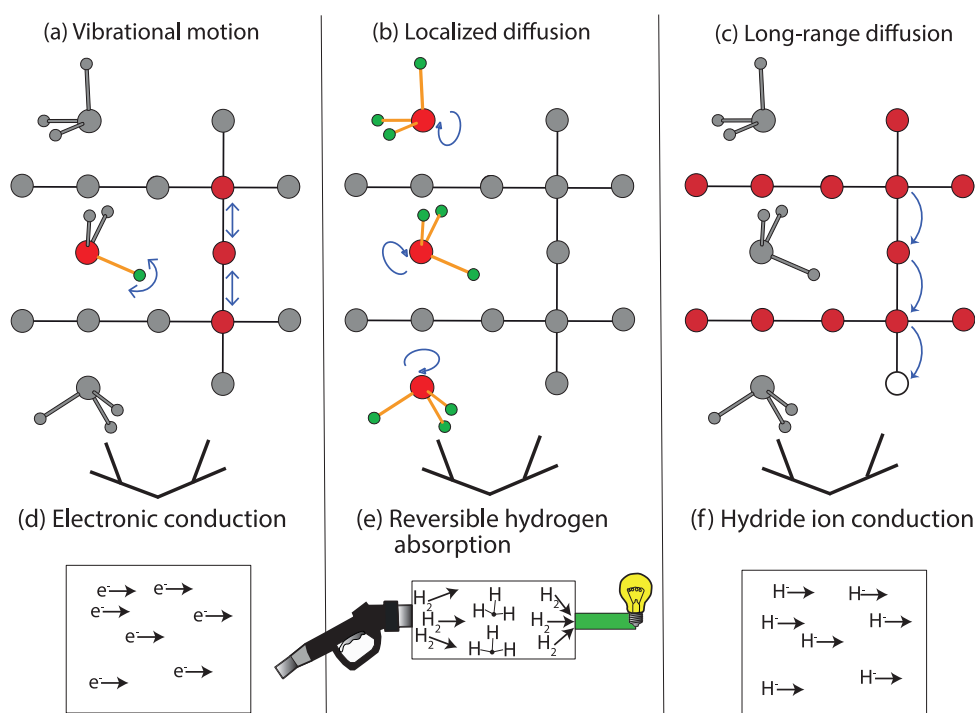


Figure 1.2: Schematic illustration of the different types of hydrogen dynamics together with the materials function relationships that have been investigated in this thesis: (a,d) vibrational motion – electronic conductivity, (b,e) localised diffusion – reversible hydrogen absorption, and (c,f) long-range diffusion – hydride ion conduction.

ergy materials", with either higher hydrogen diffusivity (for perovskite oxide materials) or hydrogen storage capacity and favourable hydrogen sorption kinetics (for alkali silanides). For this purpose, the research has been focused on the study of both local structure and dynamics - divided into vibrational motions [Fig. 1.2(a)], and localised diffusion [Fig. 1.2(b)]/long-range diffusion [Fig. 1.2(c)], respectively. These materials properties have then been correlated to the functional properties of the materials, such as electronic conductivity [Fig. 1.2(d)], hydrogen storage characteristics [Fig. 1.2(e)] and ionic conductivity [Fig. 1.2(f)]. The main tools for these investigations have involved the use of different neutron scattering techniques, especially inelastic and quasielastic neutron scattering (INS and QENS) and neutron powder diffraction (NPD), which are particularly powerful for studies of hydrogen containing materials [52].

2

Hydride structure and dynamics in solid state materials

2.1 General aspects of hydrides

A hydride is generally an extremely wide description of materials as it refers to any chemical compound in which hydrogen is combined with another element [53]. Within this broad concept there are basically three types of hydrides; saline (ionic), covalent, and metallic, which as the names suggest, are distinguished based on the type of chemical bond involved (Fig. 2.1).

Saline (ionic) hydrides form through a direct reaction with hydrogen and elements in the groups of alkali metals or alkaline-earth metals (Fig. 2.1) [54]. They exhibit general chemical formulas of MH and MH_2 where M is an alkali or alkaline-earth metal and the hydrogen is present as a negatively charged ion (H^-). Generally, these compounds are lightweight materials, which makes them useful as portable sources of hydrogen, such as sodium hydride (NaH) and calcium hydride (CaH_2) [53, 55].

Covalent hydrides form through the reaction between hydrogen and non-metals such as boron (B), Silicon (Si), and aluminium (Al) (Fig. 2.1). Ionic hydrogen species of both boron (BH_4^-) and aluminium (AlH_4^-) are extensively used as hydride sources. The cations most commonly employed are Na^+ for BH_4^- (to form $NaBH_4$) and Li^+ for AlH_4^- ($LiAlH_4$). Both compounds have

Saline Hydrides										Covalent Hydrides																									
1 H																			2 He																
3 Li	4 Be	Metallic Hydrides																5 B	6 C	7 N	8 O	9 F	10 Ne												
11 Na	12 Mg	13 Al	14 Si	15 P	16 S	17 Cl	18 Ar	19 K	20 Ca	21 Sc	22 Ti	23 V	24 Cr	25 Mn	26 Fe	27 Co	28 Ni	29 Cu	30 Zn	31 Ga	32 Ge	33 As	34 Se	35 Br	36 Kr										
37 Rb	38 Sr	39 Y	40 Zr	41 Nb	42 Mo	43 Tc	44 Ru	45 Rh	46 Pd	47 Ag	48 Cd	49 In	50 Sn	51 Sb	52 Te	53 I	54 Xe	55 Cs	56 Ba	57-71 Lanthanides	72 Hf	73 Ta	74 W	75 Re	76 Os	77 Ir	78 Pt	79 Au	80 Hg	81 Tl	82 Pb	83 Bi	84 Po	85 At	86 Rn
87 Fr	88 Ra	89-103 Actinides	104	105	106	107	108	109	110	111	112	113	114	115	116	117	118																		

Figure 2.1: Periodic table with the three types of hydride materials, based on the bonds they exhibit; saline (ionic), metallic, and covalent.

specific uses in both organic and inorganic reduction reactions and is also considered as hydrogen storage materials [53, 56, 57].

Metallic hydrides are compounds of hydrogen and transition metals (Fig. 2.1), which are typically synthesised by reacting hydrogen gas with a metal (or alloy) at high temperature. The titanium family is the most investigated one, where titanium hydride is the most stable one in air at ambient temperature [53, 58]. Not only will they form stoichiometric compounds but there is also the possibility for them to form nonstoichiometric materials, where the hydrogen atoms instead are located at an interstitial position. One, until recent, small subgroup of the metallic hydrides, is the transition metal oxyhydrides [59].

2.2 Transition metal oxyhydrides

Oxyhydrides are featured by the partial substitution of hydride ions for oxygen ions, hence the hydrogen is of hydridic nature (H^-) in the structure. Early examples of oxyhydrides are $LaHO$ [60], $Zr_5Al_3O_{0.5}H_{4.8}$ [61], $Ba_{21}Ge_2O_5H_{24}$ [62], Ba_3AlO_4H [63], MoO_xH_y [64], TiH_xO_y [65], and $12CaO \cdot 7Al_2O_3 \cdot H$ [66]. These early on oxyhydrides were often synthesised through rather complicated synthesis methods including high pressure of H_2 gas atmospheres in order to incorporate the hydride ions in the structure, which often made the material unstable and

difficult to control the amount of hydride ions. More recently, the Ruddlesden-Popper type oxyhydride $\text{LaSrCoO}_3\text{H}_{0.7}$ [59, 67] was synthesised using a novel, simpler, approach, known as the topochemical reaction [59]. This synthesis method to make oxyhydrides, discovered by Hayward *et al.* in 2002 [59] enabled future discoveries of oxyhydrides and expanding this previous rather small group of materials.

2.2.1 Topochemical reaction synthesis

Lately, the oxyhydride family of materials have significantly increased in numbers with an unanticipated discovery in 2012 by Kobayashi *et al.* [68]. They managed to synthesise a barium titanium perovskite oxyhydride through fairly simple hydride reduction (implementing the topochemical reaction with CaH_2 as previously reported by Hayward *et al.* [59] in 2002). Nedumkandathil *et al.* [69] reported about the synthesis of $\text{BaTiO}_{3-x}\text{H}_x$ in more detail, where a powder of BaTiO_3 , together with a powder of metal hydride (for example CaH_2 or NaBH_4) are used as starting materials in the topochemical reaction synthesis. The BaTiO_3 powder is mixed with the metal hydride by grinding them together in an agate mortar. The mixture is then pressed into a pellet and placed inside a stainless-steel ampoule, which is then sealed and inserted in to a fused silica jacket. The synthesis time is usually around 2 days at a temperature of about $600\text{ }^\circ\text{C}$ [69]. The metal hydride thus reduces the transition metal (Ti^{4+}) in the host material (BaTiO_3), hence creating oxygen vacancies by forming CaO . The hydrogen atoms then diffuse into the host material, now containing oxygen vacancies, and create the product material of an oxyhydride [69].

Thanks to the development of this fairly simple synthesis technique to make oxyhydrides, new oxyhydride materials have been recently synthesised. Not only were the synthesise route simplified but because the new oxyhydride exhibits a perovskite structure (ABO_3), one could easily exchange the *A*- and *B*-site atoms and hence add new compounds to this previously relatively small group of oxyhydrides. New materials include structures with transition metals such as BaScO_2H [70], SrVO_2H [71], $\text{Sr}_2\text{VO}_{4-x}\text{H}_x$ [72], SrCrO_2H [73], $\text{LaSrMnO}_{3.3}\text{H}_{0.7}$ [74] on top of the initial $\text{LaSrCoO}_3\text{H}_{0.7}$ [59] and $\text{BaTiO}_{3-x}\text{H}_x$ oxyhydrides[32, 68].

The systems $ATiO_{3-x}H_x$ ($A = Ba, Sr$ and Ca) are stable in air all the way up to *ca.* 400 °C, above which hydrogen is released, suggesting that the hydride species in $ATiO_{3-x}H_x$ have to be mobile at this temperature and possibly also below [75]. Kobayashi et al. [68] demonstrated that this material represents a versatile precursor toward a range of other mixed anion compounds such as oxynitrides [31, 76, 77], oxyfluorides [31] and even a material containing both hydride ions and protons [31].

2.2.2 Perovskite type oxyhydride $ATiO_{3-x}H_x$

Of the currently known oxyhydrides are the perovskite type oxyhydrides, $ATiO_{3-x}H_x$ ($A = Ba, Sr$ and Ca), of particular interest, because it exhibits the same structure as the suggested materials of the electrolyte in the intermediate-temperature fuel cell. The perovskite type oxyhydride of $BaTiO_{3-x}H_x$ has been the focus in this thesis.

Structural properties

In the oxyhydride form of $BaTiO_3$, *i.e.* $BaTiO_{3-x}H_x$, the O^{2-} and H^- ions form the octahedral environment around Ti in this structure, which makes the Ti atoms exist in a mixed IV/III oxidation state [68]. This change of oxidation state makes the structure bigger as it has to accommodate another electron, which will make the material cubic at all temperatures [Fig. 2.2(a)] [78]. Compared to $BaTiO_{3-x}H_x$, the pure $BaTiO_3$ instead goes through several structural changes, from a rhombohedral structure at low temperatures, through an orthorhombic structure at 183 K, to a tetragonal structure at 278 K and then to a cubic structure at temperatures above 396 K [78].

Introducing hydride ions in the oxide material will influence the characteristics significantly. For example, there will be a change in cell volume attributed to three different properties; firstly, the hydride ion has a larger atomic radius than the oxide ion (1.54 *vs.* 1.38 Å), secondly, the Ti atom gets bigger as it goes from Ti^{4+} to Ti^{3+} , and thirdly the Ti-anion bonding gets weaker and hence longer [29]. The last effect could potentially enhance chemical reaction and anionic diffusion in the oxyhydride material compared to that of the parent oxide [75]. Furthermore, when doping with hydride ions, the band

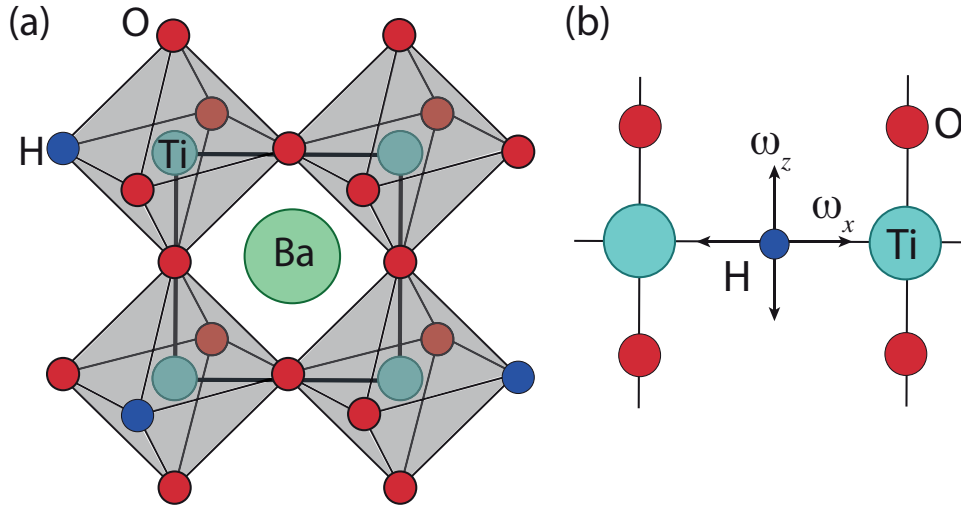


Figure 2.2: (a) Schematic figure of the cubic-structured perovskite oxyhydride $\text{BaTiO}_{3-x}\text{H}_x$ and (b) a sketch indicating the direction of the ω_{\perp} and ω_{\parallel} Ti-H vibrational motions. The hydride ion is located on a vacant oxygen site of the perovskite lattice.

gap will get narrower due to the lower electronegativity of the hydride ions (compared to oxide ions), which will increase the conductivity. Additionally, a change of bandgap will further change the possibility to absorb visible light and thus enables visible light applications for the material, such as water splitting catalysis and pigmentation [75]. An interesting feature is that the hydride ion exhibits a flexibility in size, with ionic radii of $\approx 1.30\text{--}1.53 \text{ \AA}$ found in metal hydrides. This is most probably due to the fact that the hydride ion consists of two electrons held by only one single proton, which furthermore makes the hydride ion highly adaptable to a given local environment [67, 75].

The perovskite structure, ABO_3 , of $\text{BaTiO}_{3-x}\text{H}_x$, is a relatively simple structural model that gives vast opportunities to combine different elements to achieve a range of various materials. Because the perovskite structure is so versatile, it is not only possible to exchange the anions in the materials, but also the cations (Ba for Sr and Ca) resulting in a change of various properties. For example, by changing the A -site atom in $\text{ATiO}_{3-x}\text{H}_x$ the hydrogen release temperature will change, hence the hydride ion mobility is influenced (smallest cation Ca shows the highest release temperature) [29, 30]. Also, the symmetry changes for the material, which is rather expected as the different

cations exhibits different sizes and hence introducing more or less tilt of the octahedra (smallest cation Ca shows the most tilted octahedral structure) [29]. But noteworthy is the fact that the hydride ion concentration gets higher for $\text{BaTiO}_{3-x}\text{H}_x$ in a shorter synthesis time than for the other materials. This most probably relates to the fact that Ba is a larger atom than Sr and Ca and hence results in a larger lattice for $\text{BaTiO}_{3-x}\text{H}_x$ where the O^{2-}/H^- migration more easily can take place [79].

Structurally related perovskite

The perovskite type ReO_3 belongs to a small family of undistorted cubic structures that has a completely vacant *A*-site cation in the ABO_3 perovskite structure. The structure allows vibrational modes of the rigid octahedra, which give rise to negative thermal expansion (NTE) across an extended temperature range [80–82]. ReO_3 is the only simple binary oxide that combines metallic conductivity with NTE, and it has previously been shown that the size and range of NTE observed experimentally is highly dependent on sample thermal history and method of preparation [82]. When introducing hydrogen species into the structure of ReO_3 it may occupy one or a combination of three different kinds of arrangements *i.e.* it can be covalently bonded to the oxygen atoms (forming hydroxyl groups) [Fig. 2.3(a)], but there is also the possibility to include water molecules in the cages present in the structure [Fig. 2.3(a)], and even more interesting is the fact that the Re atoms have the possibility to change oxidation number from 6+ to 5+ (even to 4+) which would, hypothetically, make it possible to create a hydride [Fig. 2.3(c)] [83–85].

Electronic properties

The presence of the extra electron in $\text{BaTiO}_{3-x}\text{H}_x$ changes the color of the material from white to blue. The cause of this colour change has been investigated by Schrader *et al.* [86], who suggested it to be due to the absorption of a specific wavelength that is attributed to a hopping process of small polarons. Polarons refer to electrons localised at specific sites, in this case on the Ti atom, rather than being delocalized within an electronic band [87]. However, there

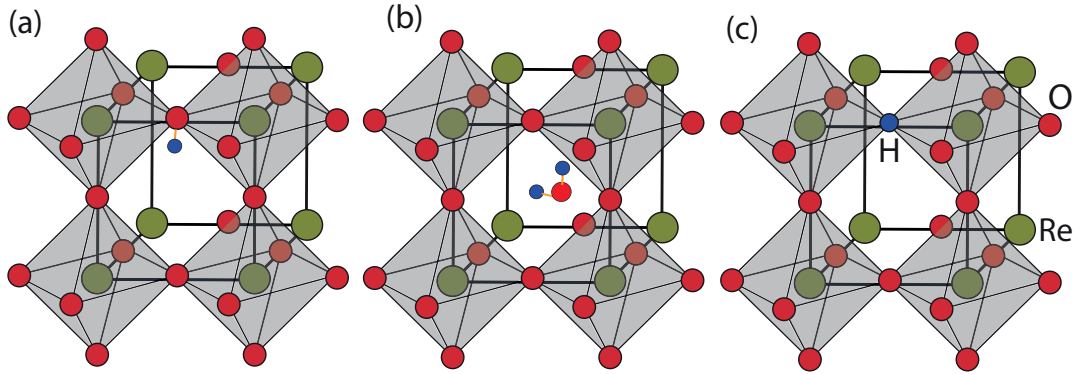


Figure 2.3: Plausible nature of hydrogen in ReO_3 : (a) hydroxyl groups, O-H, (b) water molecule at the vacant A-site, and (c) hydride ion at the oxygen position.

is still some controversy if the electron in $\text{BaTiO}_{3-x}\text{H}_x$ creates a polaron or is located within the conduction band.

In the case of $\text{BaTiO}_{3-x}\text{H}_x$, vibrational spectra may provide the answers of the behaviour and position of the extra electron. Far-infrared reflectance measurements of SrTiO_{3-x} have shown that the phonon modes are strongly influenced by the oxygen vacancies, as they get broader with increasing oxygen vacancy density [88]. Hwang *et al.* [89] observed a similar behaviour for BaTiO_{3-x} and discussed this in relation to the existence of polarons in connection to the oxygen vacancies. Furthermore, BaTiO_{3-x} shows a local structural disorder [90, 91] attributed to a polaron localised within one or several lattice sites, which perturbs the octahedra surrounding of the Ti atoms. Additionally, Raman measurements of BaTiO_3 under externally applied pressure up to 20 GPa shows that the material is not cubic but rather the presence of a tetragonal distortion of the local environment [92]. First-principal calculations on BaTiO_3 further confirm the local disorder attributed to polarons, where polarons are introduced into the structure by adding carrier electron doping from oxygen vacancies or substitutionally doped Nb^{5+} at Ti^{4+} [78]. However, including Sr in BaTiO_{3-d} rather have the opposite effect where this instead stabilises the cubic phase [93]. This could be more closer to what is observed in $\text{BaTiO}_{3-x}\text{H}_x$, where the hydride ions, similar to Sr, will stabilise the cubic structure. The same effect is observed in thin films [94, 95] and pressure studies [92] of BaTiO_3 , where the introduced strain makes it keeps its cubic structure.

First-principles calculations by Liu *et al.* [96] showed that electron polarons are responsible for the experimentally observed semiconductor-like conductivity in bulk $\text{BaTiO}_{3-x}\text{H}_x$. The distortion of the lattice associated to the polaron would then influence the local atomic environment and thereby the vibrational properties of the hydride ion. Self-trapped electron polarons in BaTiO_3 were shown to be unstable but polarons arising from the electrons donated by the hydride ions were stable on the adjacent Ti atoms hence explaining the semi-conducting properties and the blue colour of the $\text{BaTiO}_{3-x}\text{H}_x$ material [96]. Iwazaki *et al.* [87] showed that the Ti-H vibrational frequencies could be predicted in $\text{BaTiO}_{3-x}\text{H}_x$, with the help of density-functional theory calculations. Three vibrational frequencies of the hydride ions were observed, two perpendicular to the direction of the Ti-H bond (ω_{\perp}) degenerated at 854 cm^{-1} (105.9 meV), and one parallel to the direction of the Ti-H bond (ω_{\parallel}) at 1024 cm^{-1} (126.96 meV) [87]. However, these calculations make no distinctions between a polaron or an electron situated in the bandstate [87], thus the vibrational frequencies of the Ti-H vibrations remain to be measured experimentally in order to identify in which state the extra electron is situated.

By measurements on an oxyhydride film of $\text{ATiO}_{3-x}\text{H}_x$ ($A = \text{Ba}, \text{Sr}, \text{Ca}$), Yajima *et al.* [30] could detect a high electronic conductivity, hence the materials are metallic (in a bandstate configuration), even at low temperatures (2 K). The precursors, ATiO_3 ($A = \text{Ba}, \text{Sr}, \text{Ca}$), are otherwise insulating but turn into metallic conductors when hydride ions are introduced in to the structure, or more accurately when carrier (electrons) associated with the hydride ions are injected into the conduction band of the host material [79]. However, a metallic phase can be accomplished for both the BaTiO_3 and the SrTiO_3 systems through other methods, such as doping with a trivalent cation (e.g. La^{3+}) [97] at the A -site or a pentavalent cation (e.g. Nb^{5+}) [98, 99] at the Ti site. Furthermore, carriers can also be injected by introducing oxygen vacancies in the structure [79, 89, 90]. Even though the BaTiO_3 and the SrTiO_3 systems seem fairly similar, there are some differences that become apparent when doping with carriers. For example, significant lower concentrations of carrier are required in order to observe metallic conductivity for SrTiO_3 than for BaTiO_3 (10^{19} cm^{-3} compared to 10^{21} cm^{-3}). A similar behaviour was observed by Bouilly *et al.* [79] when introducing hydride ions in to the structure. $\text{SrTiO}_{3-x}\text{H}_x$ showed

metallic conductivity over the entire range of x concentrations ($0.05 < x < 0.45$), whereas $\text{BaTiO}_{3-x}\text{H}_x$ ($0.14 < x < 0.58$) exhibits semiconducting conductivity at $x < 0.2$ and only above this ($0.2 < x$) showing metallic conductivity. This is very similar to that of $\text{BaTi}_{1-x}\text{Nb}_x\text{O}_{3-}$, where the material is semiconducting at $x \leq 0.2$ which is attributed to the local distortion in the material at lower x . That is the off-centering of the $\text{Ti}^{4+}/\text{Nb}^{5+}$ site contributing to a localisation of the doped electron, hence creating a polaron [98–100]. If hypothesised that this is also true for the $\text{BaTiO}_{3-x}\text{H}_x$ material, this would imply that there is a local Ti disorder at low x contributing to a polaron and hence a semiconducting conductivity. Additionally, as these materials are films it is important to consider the miss-match between the substrate and the investigated material ($\text{SrTiO}_{3-x}\text{H}_x$ shows the smallest miss-match) [79], as this might have an effect on the electronic conductivity. The introduced strain, originating from the lattice miss-match, could similarly to the local Ti disorder, also introduce polarons in the materials and hence reduce the conductivity [79]. The question is then if it is possible to observe the polaronic effect in $\text{BaTiO}_{3-x}\text{H}_x$ and if the material shows the same local disorder as pure BaTiO_3 doped with carrier electrons.

Hydride ion conduction and dynamics

Kobayashi *et al.* [68] showed, through deuterium exchange of the hydride ions in $\text{BaTiO}_{3-x}\text{H}_x$ at 400 °C, that the hydride ions have to be mobile (Fig. 2.4). This finding is highly exciting because it implies that the perovskite structural framework can accommodate both, cation (proton) and anion (hydride) conduction. In particular, interesting diffusion mechanisms specific to hydride-ions may exist in this material.

In a fairly recent article from 2017, Tang *et al.* [101] used deuterium exchange to investigate the hydride diffusion in $\text{BaTiO}_{3-x}\text{H}_x$ and $\text{LaSrCoO}_3\text{H}_{0.7}$. They found that there is indeed a dependence on x for the hydride diffusion in $\text{BaTiO}_{3-x}\text{H}_x$. When x is low ($x < 0.4$), the migration of hydride ions in $\text{BaTiO}_{3-x}\text{H}_x$ is featured by a relatively high E_a of 3.8 eV and hence the hypothesis is that it requires the simultaneous movement of oxide ions (E_a of oxygen diffusion in $\text{BaTiO}_3 \approx 2$ to 2.8 eV [102–107]). When x is high ($x > 0.4$), they measured a much lower E_a of 2 eV and hence the hydride ions may form a

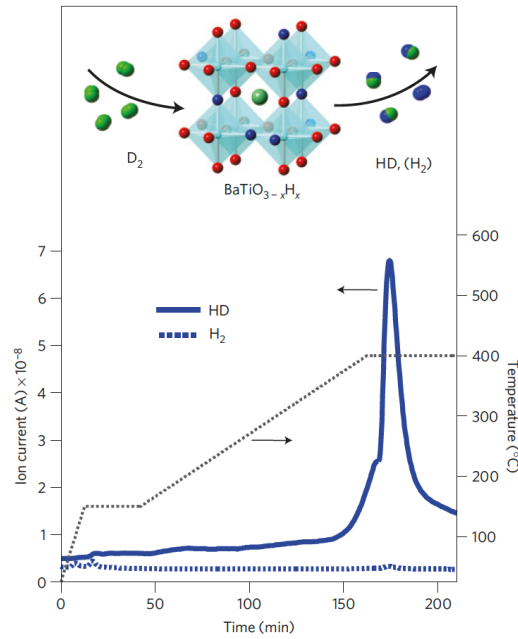


Figure 2.4: Mass spectrometry of gaseous species during deuteride exchange. $\text{BaTiO}_{3-x}\text{H}_x$ is heated in D_2/Ar , while gaseous products are monitored. The black dotted line plots the temperature as a function of time. Reprinted by permission from Springer Nature: *Nature Materials*, "An oxyhydride of BaTiO_3 exhibiting hydride exchange and electronic conductivity", Kobayashi *et al.* [68], ©(2012).

conduction pathway not dependent on the movement of oxygen ions. Results from simulations [101] showed a large probability that there is not only nearest neighbour (NN) jumps (Fig. 2.5) but most probably the diffusional motion is a mix between NN jumps and second nearest neighbour (2NN) jumps. In order to fully investigate the true jump distance in $\text{BaTiO}_{3-x}\text{H}_x$ they pointed out that QENS measurements on the material is needed. Although, the article [101] also includes a deuterium exchange measurement of $\text{LaSrCoO}_3\text{H}_{0.7}$, where a comparison to previous QENS measurements was possible [108]. Thus, they found a big difference in E_a , where the QENS study on $\text{LaSrCoO}_3\text{H}_{0.7}$ showed an E_a of around 0.2 eV [108], whereas the deuterium exchange measurements showed an E_a of roughly 2 eV, that is 10 times higher than for the QENS measurement. This is an inconsistency but one has to consider that these two experiments measure different characteristics, the gaseous deuterium exchange experiments measure a chemical diffusion coefficient, as it depends on

the chemical potential between the gas and solid phase, while QENS yields the pure bulk self-diffusion coefficient of the hydride ions. So the gaseous deuterium exchange experiments might be a more realistic measurement where several variables are included (such as surface and grain boundaries effects). QENS is on the other hand a more reliable measurement to study the actual diffusional motion and how it depends on the material at hand.

Ionic conduction in related oxyhydrides

Pure H^- conductivity have been measured by Kobayashi *et al.* [25], who showed a relatively low E_a of ≈ 0.7 eV at 590 K when introducing anion vacancies in the oxyhydride material. This was however not $\text{BaTiO}_{3-x}\text{H}_x$ but rather $\text{La}_{1-x}\text{Sr}_{1+x}\text{LiH}_{2-x}\text{O}_2$ ($x = 0.1, 0.2, 0.3$ and 0.4), a material that sufficiently provide electron-donating cations situated in a sublattice in order to assure an observation of H^- conduction. The measurement would otherwise most probably be dominated by electron conduction, hiding the hydride ion conductivity. An important conclusion from this paper is that the diffusional motion of the hydride ion can be even further promoted by introducing oxygen vacancies in the perovskite structure, this in accordance with recent anion exchange studies [77, 109]. Mikita *et al.* [77] showed that the hydride ions in $\text{EuTiO}_{2.82}\text{H}_{0.18}$ enables a N^{3-}/H^- exchange at 400 °C, creating a material containing oxygen vacancies ($\text{EuTiO}_{2.82}\text{N}_{0.12}\square_{0.06}$). This material could then further go through ammonolysis in two steps with two different temperatures (600 and 800 °C) to finally create the fully oxidised material of EuTiO_2N . Direct ammonolysis from EuTiO_3 to EuTiO_2N was not possible, suggesting that the hydride ions in a combination with the oxygen vacancies enables this full oxidation. The reason why N^{3-} needs a higher temperature than H^- (800 °C compared to 600 °C) for the topochemical ammonolysis is related to the less mobile nature of N^{3-} , due to its higher valence. Takeiri *et al.* [109] looked explicitly at the hydride/oxide exchange in SrTiO_3 , and observed that only a small amount of oxygen vacancies was needed in order to promote the exchangeability and hence increase the anion (O^{2-}/H^-) diffusivity. The lower anion exchangeability in pristine SrTiO_3 and CaTiO_3 means that the smaller lattices of these compounds compared with BaTiO_3 substantially restrict the anion (O^{2-}/H^-) diffusion. Hence an amount of oxygen vacancy doping would be necessary in

order to achieve the same composition with a high amount of hydride ions as for BaTiO_3 ($\text{BaTiO}_{2.4}\text{H}_{0.6}$).

Interestingly, Bridges *et al.* [108] detected a long-range jump diffusion for the hydride ions in $\text{LaSrCoO}_3\text{H}_{0.7}$. The hydride-ion hopping mechanism was found to initiate in the temperature range used for synthesis of the material and occurs in conjunction with loss of hydrogen from the sample. The resulted jump distance fitted well with that of the structure and gave approximately the distance between hydrogens. The obtained activation energy (E_a) and hydride-ion diffusion coefficient (D) were *ca.* 200–230 meV and 6×10^{-5} – $10 \times 10^{-5} \text{ cm}^2\text{s}^{-1}$ in the temperature range of 700–750 K [108]. These results are in accordance with recent first principles calculations, investigating the transport of hydride ions in $\text{BaTiO}_{3-x}\text{H}_x$, which show a low activation energy (0.28 eV) of vacancy assisted diffusional motion [96]. This low activation energy could be attributed to the relatively weak interactions between the hydride ion and the transition metal, and also its smaller mass and charge compared to the O^{2-} anion.

The dynamics of the hydride-ions in $\text{BaTiO}_{3-x}\text{H}_x$ are, as mentioned, not directly measured, but two main possible diffusional routes for the hydride ion in $\text{BaTiO}_{3-x}\text{H}_x$ have been discussed, i) oxygen vacancy assisted diffusion, and ii) transformation into a proton and then interstitial diffusion to an empty lattice point, followed by a conversion back to a hydride [68, 87, 96, 110, 111]. Results from computer simulations show that E_a for interstitial diffusion of protons in BaTiO_3 takes on a value of *ca.* 0.2 eV [110], whereas results from QENS studies of acceptor doped perovskite materials, supported by computational techniques, show activation energies typically in the range 0.1 to 0.2 eV for diffusional motions of protons [19, 112–118].

For oxygen vacancy assisted diffusion of the hydride ion [i)], it has been hypothesised that when x is low, the migration of hydride-ions depends on the movement of oxide-ions, which is featured by a quite high activation energy (~ 0.8 eV), whereas when x is high, the concentration of hydride-ions is so high that the hydrogens may form a conduction pathway not dependent on the movement of oxygen ions (Fig. 2.5) [68]. If this is the case, the question is if there is an optimum hydride-ion concentration? Another important variable to consider is how the diffusional motion of the hydride ion can be even further promoted by introducing oxygen vacancies in the perovskite structure, this in

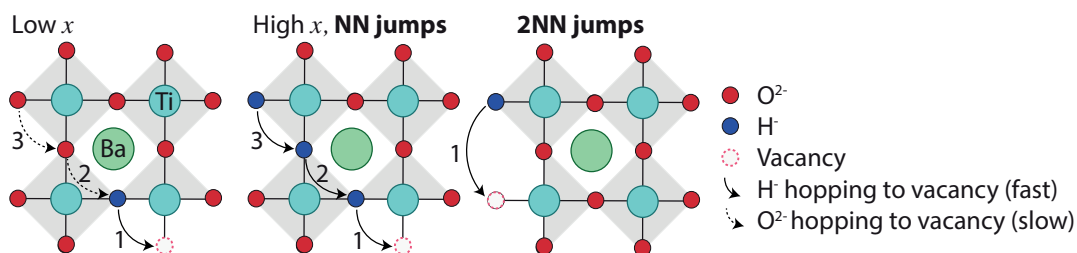


Figure 2.5: Schematic figure of when x is low, the migration of hydride-ions depends on the movement of oxide-ions, whereas when x is high, the concentration of hydride-ions is so high that the hydrogens may form a conduction pathway not dependent on the movement of oxygen ions. The figure also shows the nearest neighbour (NN) jumps and second nearest neighbour (2NN) jumps in the $\text{BaTiO}_{3-x}\text{H}_x$.

accordance with recent anion exchange studies [77, 109]. Overall, both oxygen vacancy concentration and mobility would probably heavily influence the hydride ion transport in oxyhydrides. Such information will provide new input into hydrogen dynamics in perovskite materials generally, now stretching from protic to hydridic species.

2.3 Metal and complex hydrides

2.3.1 Metal hydrides

Properties of the metal hydrides

Metal hydrides typically store hydrogen at 4-8 wt.%, not including storage vessel or other storage system requirements [119]. The structure of metal hydrides is usually limited to the compositions MH , MH_2 , and MH_3 , with the hydrogen atoms fitting into octahedral or tetrahedral holes in the metal lattice, or a combination of the two [120]. However, as a hydrogen storage material, metal hydrides usually exhibit either a too low gravimetric capacity or a too high decomposition temperature. In comparison, the hydride alloys of CoNi_5H_4 and LaNi_5H_6 fall inside the targeted operational window, when it comes to temperature and pressure, but their gravimetric capacity is too low for on-board hydrogen storage, *e.g.* 1.1 and 0.9 wt.%, respectively. On the other hand, MgH_2 has a large hydrogen content (7.6 wt.%) but its decomposition temper-

ature is too high (330 °C) [121]. Nonetheless, the thermodynamics can be improved for metal hydrides by adding a chemical species that either destabilises the hydrogenated state or stabilises the dehydrogenated state, referred to as destabilisation (of the system) [121, 122].

Another important factor to consider is the kinetics of the hydrogen uptake (hydrogenation) and release (dehydrogenation), which is usually slow but can be improved by adding a catalyst. The rate of hydrogenation is controlled by three (main) factors, (i) the rate of the dissociation of the hydrogen molecules at the surface, (ii) the difficulty in penetration of the hydrogen from the surface into the metal, and (iii) the hydrogen diffusion through the hydride layer already formed and into the bulk of the material. The rate of dehydrogenation is instead influenced by, (i) the chemical and structural changes of the bulk material, (ii) the transferring of hydrogen from the bulk to the surface (bulk diffusion) and (iii) the recombination of the hydrogen atoms on the surface [121]. A catalyst could then be used to enhance these kinetic properties by decreasing the activation energy barriers and therefore improve the rate of both hydrogenation and dehydrogenation [122].

Making nano-sized particles of the hydrogen storage material, has also shown some effect in improving the kinetics. The reasons for this should be that a nano-sized particle shows an enlarged solid/gas interface but also shortens the hydrogen diffusion paths. Additionally, nanoparticles (in the presence of hydrogen) usually gain an increased lattice constant, hence contributing to a larger interstitial volume for hydrogen storage [121, 122].

The MgH₂ material

The metal hydride of MgH₂ is one of the binary hydrides that still attracts considerable attention owing to its light weight, low cost and high gravimetric density (7.6 wt.%) even given the fact that it suffers from slow kinetics and thermodynamic limitations for storage (a high decomposition temperature of 330 °C). Efforts to speed up the kinetics have been done through the reduction of particle size (by ball milling), alloying and doping [123]. For example, Hanada *et al.* [124] showed that milled and Ni-doped MgH₂ reduced its decomposition temperature to 150–250 °C while containing a hydrogen wt% of 6.5. Furthermore, a remarkable improvement in absorption was reported by

the same group [125] for Nb₂O₅ doped and milled MgH₂ with high desorption kinetics at 160°C under a helium flow [123]. With the development of suitable catalysts, the charge-discharge times has drastically been reduced, however the thermodynamics of the process still lacks behind. Li *et al.* [126] showed that the kinetics of hydrogen absorption-desorption could be improved by instead synthesise nanowires of Mg. Enhancement through nanostructuring with the introduction of defects during loading and release of hydrogen in MgH₂ was studied by neutron scattering [127]. The results showed that by using small quantities of Nb and V, that acts as catalysts during the hydrogenation process, the temperature could be decreased. The improvement in the kinetics was attributed to the presence of vacancies. Further INS experiments of the same material were consistent with that interpretation [128, 129].

2.3.2 Complex hydrides

Properties of the complex hydrides

One subgroup to the metal hydrides is the complex hydrides that consist typically of alkali or alkaline earth elements that are ionically bonded to a complex anion. The anions themselves can consist of light metals group 1, 2, 3, e.g. Li, Na, B and Al, to which hydrogen is covalently bonded [38, 120]. The main difference between the complex and metallic hydrides is the transition to an ionic or covalent compound upon hydrogen absorption. The hydrogen in the complex hydrides is often located in the corners of a tetrahedron with for example B or Al in the centre [120]. The expanding list of promising complex hydrides for hydrogen storage applications include materials such as amides $M(\text{NH}_2)_x$, imides $M(\text{NH})_{x/2}$, borohydrides $M(\text{BH}_4)_x$, alanates $M(\text{AlH}_4)_x$ and $M_x(\text{AlH}_6)_y$, which are already well investigated in the literature, and also the recently investigated amido-boranes $M(\text{NH}_2\text{BH}_3)_x$, ammonium-closo-borane $(\text{NH}_4)_2\text{B}_{12}\text{H}_{12}$ and hydrazinido-boranes $M(\text{N}_2\text{H}_3\text{BH}_3)_x$ [130–142]. The focus has been to find lightweight materials for optimum gravimetric hydrogen densities. Hence materials that are lithium- and sodium-based, and variations of the nitride-imide-amide system have been extensively studied for this purpose [120, 138, 143, 144]. Of particular interest are LiBH₄, NaBH₄, and NaAlH₄.

The NaAlH₄, NaBH₄ and LiBH₄ materials

NaAlH₄ is a relatively lightweight material, but as for all alanates, there is an issue with achieving reversibility [138]. Hence, high pressure is needed (130-150 bar at 170 °C) in order to reload the hydrogen into NaAlH₄. A cyclic test showed that Ti-doped NaAlH₄ improved the reversibility and can thus preform dehydrogenation and then hydrogenation several times (35 cycles), but with the cost of a decrease of hydrogen storage capacity, going from 4.2 to 3.1 wt.% [138]. However, the rate of dehydrogenation/hydrogenation was still too low and the operating temperature still too high (>160 °C). A number of studies employing different catalysts have been undertaken, one of which reports about a most potent catalyst, TiCl₃ [143, 145]. Anton [146] showed that the cation radii of the dopant cation is the most important factor affecting the dehydrogenation process, where a midpoint (0.74 Å close to that of Ti³⁺ of 0.76 Å) between the ionic radii of Al³⁺ and Na⁺ is optimum [143, 146]. A more detailed study of NaAlH₄ with this improved catalyst was conducted [120, 139] and a desorption hydrogen pressure of 2 bar at 60 °C was found for the first (3.7 wt.% H) and second (3.0 wt.% H) dissociation steps. Additionally, carbon nano tubes have also shown good promise as a dopant, improving the recovering of the storage capacity to 4.2 wt.% [147] and accelerating the dehydrogenation [148]. To increase the gravimetric and volumetric hydrogen capacity even further a reasonable step is to exchange Al to B and hence investigate the borohydrides [143].

NaBH₄ is a material that is even more lightweight than NaAlH₄ but the material is stable in dry air, thus an amount of water is needed in order to achieve dehydrogenation. However, DOE has given a target amount of the water content on the hydrolysis in order for the material to be integrated properly in the fuel cell system [143]. Therefore, the use of catalysts (for example Pt-LiCoO₂, NiCl₂, Al and carbon nanotube paper) and salts (for example NaOH) is crucial to achieve an efficient dehydrogenation with as little water as possible [143]. Total hydrogen evolution could be enhanced up to a total of 6.5 wt.% at 45 °C, out of which 4 wt.% is at room temperature, using a non-noble catalyst Ni_xB [149]. An extensive knowledge of the dynamics in the materials could further enhance dehydrogenation and hydrogenation. NaBH₄ undergoes

an order-disorder transition near 190 K. Below this temperature, the compound exhibits a tetragonal lattice with orientationally ordered BH_4^- anions. Above the temperature of 190 K, the material transforms into a face-centred-cubic (fcc) structure with orientationally disordered BH_4^- anions. Each anion possesses two equally probable orientations superimposed to form a cube of eight H atoms, each with 50% occupancy, with a B atom at the center [150]. In the cubic phase of NaBH_4 , the motion of the BH_4^- ion is dominated by 90° reorientations. Within the ionically bound alkali borohydrides, the BH_4^- anions are not fixed. The BH_4^- motions are thermally activated and characterised by activation energies in the order of 0.1 eV, typical frequencies are in the terahertz range at temperatures of about 400 K [151]. Furthermore, the BH_4^- reorientational mobility in the high-temperature disordered phase of NaBH_4 was investigated by partial substitution of the BH_4^- anion with either smaller Cl^- or larger I^- anions. This to possibly change the local dynamics and hence lower the temperature of the dehydrogenation. The study showed an increase in BH_4^- anion mobility due to the increase of the fcc lattice constant hence increasing the available volume for the BH_4^- anion to move. Additionally, some differences in BH_4^- reorientational mechanisms were observed for $\text{NaBH}_4\text{-NaCl}$ and $\text{NaBH}_4\text{-NaI}$. The former displaying more cubic tumbling behaviour, similar to that of pure NaBH_4 , and the latter more tetrahedral tumbling behaviour [150]. In order to learn more about the dehydrogenation, hence the dynamics of the borohydrides, it is reasonable to investigate the influence that the alkali atom have on this process. Hence the next step would be to look at the even more lightweight material of LiBH_4 .

LiBH_4 then shows a favourable hydrogen mass fraction (0.185), but a somewhat unfavourable hydrogen-cycling behaviour [136]. The desorption process can be catalysed by adding SiO_2 and significant thermal desorption has been observed, starting at 100°C [120, 152]. Additionally, efforts have been made to put this molecule in different confinements to improve the thermodynamics, kinetics and reversibility of hydrogen absorption/desorption in LiBH_4 . These confinements have consisted of different solutions such as nanopores, mixing with MgH_2 , and mixing with Li halide salts [136], in order to change the localised dynamical behaviour. The rotational behaviour of BH_4^- ions in cubic ABH_4 phases involves dynamics of rotational jumps of the molecules about the

high-symmetry axes, that is 90° reorientations around the three C_2 axes (resulting in a cubic H environment around the B atoms) and 120° rotations around the four C_3 axes [136]. In a structure like this, the reorientations around any particular axis are very rapid but a jump reorientation of the entire axis are usually much slower. This may be related to the unfavourable thermodynamic behaviour that bulk LiBH_4 exhibits. However, when LiBH_4 is instead put in a nanoconfinement of carbon scaffolds, the molecular reorientations change and go from localised jump motions to a uniaxial rotational diffusion [137]. Hence, the thermodynamic behaviour changes for LiBH_4 and the hydrogen absorption/desorption process is improved [134–137, 153].

Difficulties with the reversibility is still quite common in the lightweight complex hydride materials such as LiBH_4 and LiAlH_4 [27]. Hence an option is then to learn more about hydride mobility and transport in a material which show excellent reversibility, such as ASiH_3 , even though it is gravimetrically more unfavourable.

2.3.3 The ASiH_3 material

Structural properties

At room temperature, the crystal structure of ASiH_3 corresponds to an average cubic NaCl-type arrangement of alkali metal and Si atoms, meaning that pyramidal SiH_3^- anions are distributed in random orientations in the crystal structure (α - ASiH_3) [47, 154, 155]. The structure suggests a quasi-spherical arrangement with 24 sites of preferred orientations for the hydrogen atoms around each Si atom (Fig. 2.6). At temperatures below 200 K, ASiH_3 compounds exist as hydrogen-ordered β modifications [44, 47, 48, 156], where β - KSiH_3 phase exists as an orthorhombic $Pnma$ structure, and β - RbSiH_3 and β - CsSiH_3 phase as a monoclinic $P2_1/m$ structure [47, 157]. The difference in β -phase structure for KSiH_3 compared to RbSiH_3 and CsSiH_3 is attributed to the distortion of the low temperature structure when accommodating the larger cations of Rb^+ and Cs^+ . On the basis of differential thermal analysis on KSiH_3 , a reversible phase transition was observed between the high-temperature α -phase and low-temperature β -phase on cooling (273–278 K) and the reverse (β to α) on heating (288–293 K), thus indicating some hysteresis in the material [156].

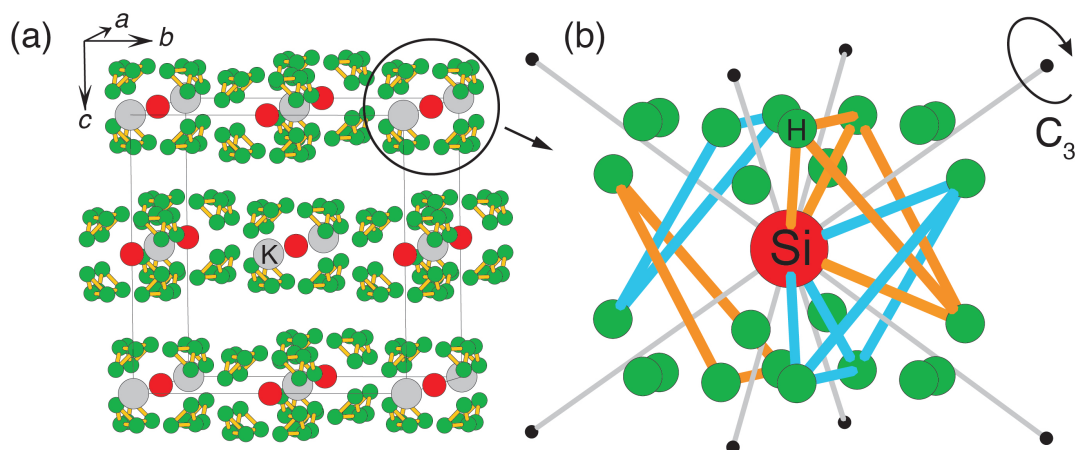


Figure 2.6: (a) Structural model for disordered α -KSiD₃ representing a cubic NaCl-type arrangement of K and Si atoms (space group $Fm\bar{3}m$). H atoms distribute according to a $96k$ Wyckoff site (occupancy 12%). This yields a quasi-spherical environment of 24 H atom positions around each Si atom. (b) The 24 H atom environment as a consequence of aligning pyramidal SiH_3^- ions (with respect to their C_3 axis) randomly along the four body diagonals of the cubic unit cell (grey lines). This yields eight possible orientations of which four (two "up" and "down" alignments) are emphasised in the figure (light blue and orange bonds).

However, for RbSiH₃, a triclinically distorted structure have shown to provide a better fit in neutron powder diffraction (NPD) measurements just close to the phase transition, suggesting that the transition is even further complicated [158].

Kranak *et al.* [48] observed a quite unusual behaviour of the Si-H bond in ASiH₃ ($A = \text{K}$ and Rb), where the bond strengthened as the material goes from the ordered β -phase to the disordered α -phase. Furthermore, a rather large molar volume difference (about 15%) was also observed for the same transformation compared to other complex hydride systems (around 5%) [48, 158]. The hydrogenation of the ASi ($A = \text{K}$, Rb and Cs) Zintl phases gives alkali metal silyl hydrides ASiH₃ ($A = \text{K}$, Rb and Cs), which are able to store up to 4.3, 2.6 and 1.85 wt. % of H₂, respectively. Additionally, the hydrogenation process is reversible in a good P - T window; a 0.1 MPa hydrogen equilibrium pressure can be obtained at around 414 K, which is compatible with proton exchange membrane fuel-cell applications [44, 47, 159, 160].

Dynamical properties

The favourable thermodynamic characteristics of α -ASiH is due to an unusually low entropy variation over the hydrogen absorption/desorption process. This has been attributed to the disorder in α -ASiH₃, whose structural properties actually correspond close to that of a slightly compressed gas-phase species (Si-H bond length = 1.52 Å; H-Si-H angle 92.2°). Actually, Kranak *et al.* [48] proposed that SiH₃⁻ ions in the disordered α -ASiH₃ relates closely to a freely rotating ion with vibrational properties similar to a silyl ion in a polar solvent. Furthermore, Mink *et al.* [161] could clearly see drastically widened lines in the Raman spectra, profoundly suggesting dynamical disorder, especially in the high temperature α -phase. Moreover, the SiH₃⁻ ions in β -RbSiH₃ showed to be less restricted compared to the SiH₃⁻ ions in β -KSiH₃, explaining why RbSiH₃ is exhibiting a lower phase transition temperature, 279(3) and 300(3) K (when increasing the temperature) for RbSiH₃ and KSiH₃, respectively [158, 161].

On the basis of the background given, the knowledge about the dynamical behaviour of the reorienting molecule can help to design new, improved hydrogen storage materials.

3

Methodology

3.1 General aspects of neutron scattering

Neutron scattering is a powerful and versatile experimental technique, used to investigate the structure and dynamics in materials. Neutrons have wavelengths and energies similar to interatomic distances and atomic motions in condensed matter, which make it possible to investigate both the atomic-scale structure and dynamics of materials with neutron scattering techniques. The versatility of the neutron scattering techniques is utilised by a wide range of sciences, such as condensed matter physics, materials science, chemistry, biology, engineering, geology and cultural heritage [162].

Neutrons are subatomic particles with no net electric charge, and their interaction with matter occurs via scattering on the atomic nuclei. This is different from the scattering of other particles such as protons and electrons, which have an intrinsic electric charge and instead interact electromagnetically with matter. The neutron-nuclei interaction is in general weak and bestows the neutron probe with a unique ability to penetrate deep into the bulk of many solid materials [163]. The fact that the interaction is weak also makes neutron scattering a non-invasive technique, where delicate and sensitive materials will stay unharmed. However, the downside of this weak interaction is that it also makes neutron scattering to a "slow" and expensive tool. Additionally, neutron scattering instruments exhibit a low flux compared to other techniques, for example those based on X-rays. This is due to the low flux from the neutron

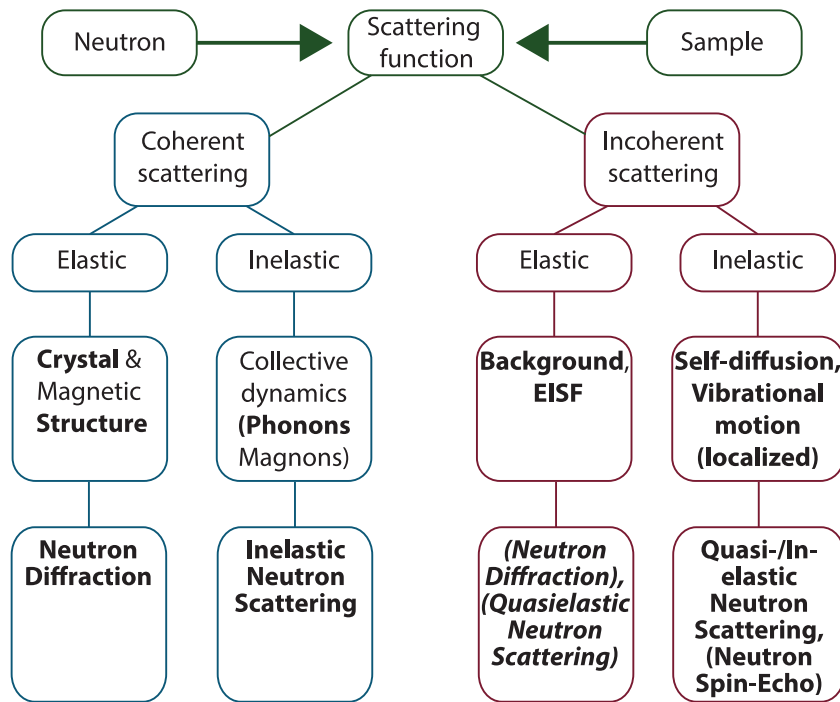


Figure 3.1: The scattering function, obtained from neutron scattering experiments and the different characteristics of this function together with the information that can be obtained.

source itself, but also that the beam generally needs to be monochromatized, hence the flux is reduced even further. Thus, measurements are generally long and neutron scattering should only be used when the use of other particles, such as photons or electrons, which often are more readily available, are inadequate [162]. A specific example of materials for which X-rays and electron techniques are inadequate, are those containing hydrogen. This is because photons and electrons do not have the possibility to detect hydrogen atoms, since they primarily interact with the electron shells (which are very small for hydrogen atoms). In contrast, the efficiency of neutron scattering is instead decided by the scattering cross section that tells us how well the neutron will scatter on a specific atomic element. The scattering cross section does not show any linear dependence on the atomic number (such as for X-rays and electron interactions), but the cross section for hydrogens by neutrons is considerable large. Neutron scattering is therefore a very powerful tool, compared to other techniques, to observe hydrogen in solids [164].

The obtained quantity in most neutron scattering experiments is the so called "scattering function", which describes how (*i.e.*, in which direction and with which energy) the incident neutrons are scattered on a material (this is further explained in section 3.3 and 3.4). The scattering function may be divided into a coherent and an incoherent part, as well as inelastic and elastic contributions, see Fig. 3.1 [165].

Coherent scattering, gives information about the average crystal structure and collective dynamics in the material. Incoherent scattering gives information about local structure and atomic self-dynamics. Depending on the aim of the study, either the elastic (interaction without any change of energy) or inelastic (interaction with an energy loss or gain) scattering is analysed. The bold texts in Fig. 3.1 are the characteristics and the corresponding experimental techniques that have been used and will be discussed in this thesis.

3.2 Neutron diffraction

Neutron diffraction is utilised to measure the structure of a material, and it is even possible to distinguish between different isotopes, but more importantly, it is also possible to detect hydrogen atoms.

For an elastic scattering event (Fig. 3.2) the following applies

$$k = |\mathbf{k}| = |\mathbf{k}'| = k' = \frac{2\pi}{\lambda}, \quad (3.1)$$

where k and k' are the wave numbers (\mathbf{k} and \mathbf{k}' are the wave vectors) of the incident and scattered wave, respectively. Because there is no change of energy between k and k' , the wave number is preserved and hence the wavelength of the incident neutrons (λ) will not change at the scattering process [166]. Furthermore, the scattering vector, \mathbf{Q} , is defined as

$$\mathbf{Q} = \mathbf{k}' - \mathbf{k}. \quad (3.2)$$

The momentum lost from the neutron at collision is the momentum transfer, $\hbar\mathbf{Q}$, which comes from the particle-wave dualism defined by de Broglie [165]. The momentum of the particle corresponds to a wave with wave vector \mathbf{k} , given

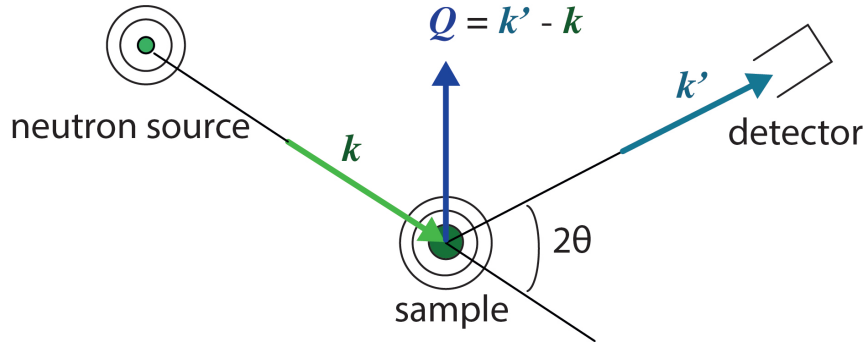


Figure 3.2: Schematic drawing of a neutron that is elastically scattered on a sample.

by $\mathbf{p} = \hbar\mathbf{k}$. Applying trigonometry on the scattering event, the following can be deduced about the magnitude of \mathbf{Q}

$$|\mathbf{Q}| = Q = \sqrt{k^2 + k'^2 - 2kk' \cos 2\theta} \Rightarrow Q = \frac{4\pi}{\lambda} \sin \theta. \quad (3.3)$$

The measured quantity in a diffraction experiment is the intensity distribution of the scattered neutrons as a function of the scattering vector, $Int(\mathbf{Q})$. The intensity is proportional to the cross section and the magnitude of Q related to the neutron wavelength and scattering angle according to Eq. 3.3 [165]. Fig. 3.3 shows, as an example, neutron diffraction data of the oxyhydride, $BaTiO_{3-x}H_x$, as measured on the D2B diffractometer at ILL [167]. The Rietveld method is used on the observed diffraction pattern, where a full profile fitting is conducted [168]. This includes using a least-square refinement technique, where a computer-generated profile of an assumed structure is fitted to the diffraction data. The results show that $BaTiO_{3-x}D_x$ ($x = 0.6$) exhibits a majority of a cubic phase (9% tetragonal and 91% cubic), whereas $BaTiO_{3-x}D_x$ ($x = 0.07$) exhibits a majority of a tetragonal phase (64% tetragonal and 36% cubic), suggesting that a certain amount of hydride ion concentration is needed in order to accomplish the cubic structure [29, 69].

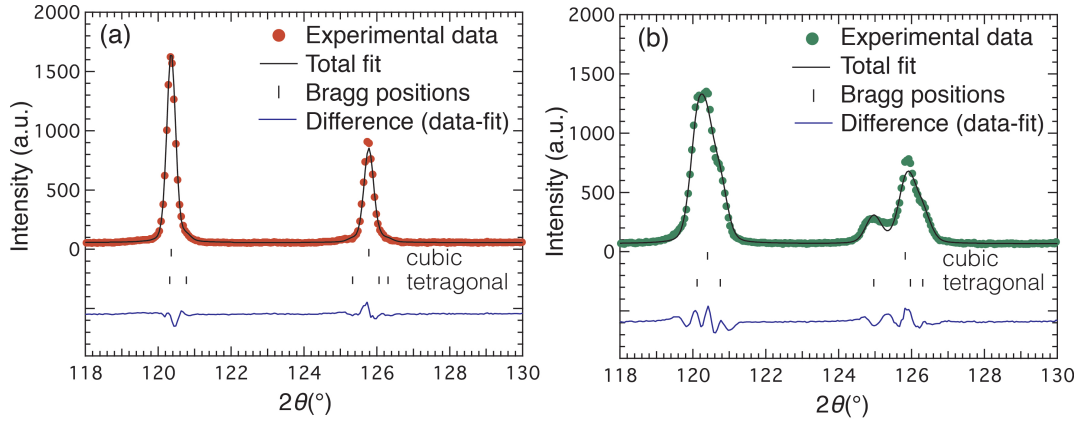


Figure 3.3: Diffraction pattern of (a) $\text{BaTiO}_{3-x}\text{D}_x$ ($x = 0.6$) and (b) $\text{BaTiO}_{3-x}\text{D}_x$ ($x = 0.07$), together with the Rietveld refinement with a calculated pattern for the cubic and tetragonal structure.

3.3 Inelastic neutron scattering

INS gives the opportunity to not only study the structure of the material but also the dynamics. INS accesses the intermediate range of time (~ 0.5 ps to 1 μs) and space (~ 0.5 to 800 nm) where many of the interesting dynamical processes in materials are taking place [165, 169]. In addition, INS is not subjected to any optical selection rules (otherwise applied to Raman and infrared spectroscopy), so, in the case of vibrational motions, all vibrations are in principle measurable. The reason for this is that INS is dependent on the neutron cross-section of the atoms and not from changes in the electronic properties of the molecule that occur as the vibration is excited, as in the case for Raman and infrared spectroscopy [170].

The discussion in the previous section on diffraction assumed that the neutron, at collision, preserved its energy, however, with INS the neutron can either preserve, gain or lose energy when interacting with the atoms of the material, which is depicted in Fig. 3.4. Now, because $k \neq k'$, Eq. 3.3 will change to

$$Q = \sqrt{k^2 + k'^2 - 2kk' \cos 2\theta} = \sqrt{\frac{8\pi^2}{\lambda^2} + \frac{2m\omega}{\hbar} - \frac{4\pi}{\lambda} \sqrt{\frac{4\pi^2}{\lambda^2} + \frac{2m\omega}{\hbar}} \cos 2\theta}. \quad (3.4)$$

In this new equation, Q is dependent on the energy, $\hbar\omega$, hence Q is no longer constant for a single scattering angle. In the scattering process the energy and

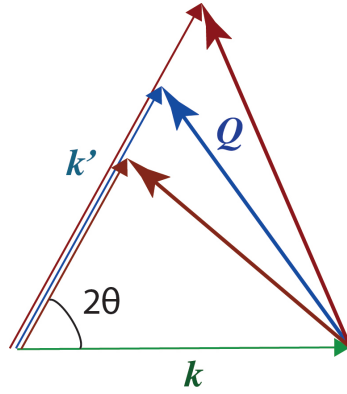


Figure 3.4: The difference in scattering vector, \mathbf{Q} , depending on if the scattering is elastic (blue) or inelastic (red), that is the neutron gains (big triangle) or loses (small triangle) energy. The scattering vector is the resulting difference between the incident and the final wave vector, \mathbf{k} and \mathbf{k}' , respectively.

momentum are therefore conserved, thus the energy and momentum exchange are expressed as $\hbar\omega = E' - E$ and $\mathbf{Q} = \mathbf{k}' - \mathbf{k}$, respectively. Here, E is the incident energy of the neutron, whereas E' is the energy of the scattered one.

3.3.1 Mean-square displacement

Examples of processes giving rise to inelastic scattering are phonons [Fig. 1.2(a) right], local vibrational modes [Fig. 1.2(a) left] and local and translational diffusions of atoms [Fig. 1.2(b) and (c)]. Phonons refer to the vibrations of the lattice and can be treated as quasiparticles with a specific energy. Hence the scattering process can be viewed as a collision between phonons and neutrons, which will result in specific energy excitations.

An important aspect to discuss is how the phonons affect the elastic scattering, which is described by the Debye-Waller factor [165]. This factor can be explained with a 'hand-waving' argument: atoms are displaced by a vector u_j from their nominal lattice position due to the thermal vibrations. The value of $\langle u \rangle$ is on average zero, but there will be a finite mean-square displacement (MSD) $\langle u^2 \rangle$. The Debye-Waller factor can be shown to be [165]

$$\exp(-\langle (\mathbf{Q} \cdot \mathbf{u}) \rangle) = \exp(-Q^2 \langle u^2 \rangle / 3). \quad (3.5)$$

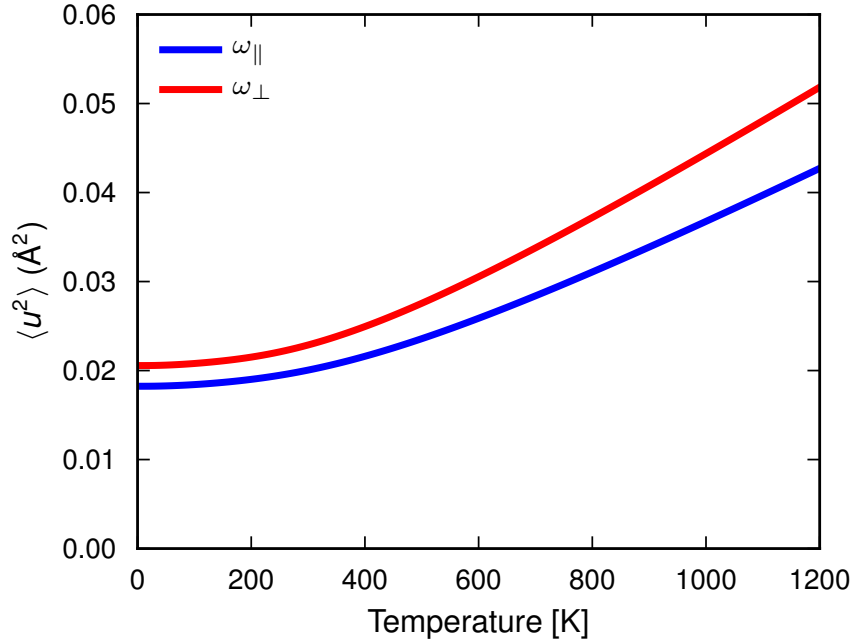


Figure 3.5: Temperature dependence of the MSD of Ti-H vibrations (ω_{\perp} in red and ω_{\parallel} in blue) in $\text{BaTiO}_{3-x}\text{H}_x$, as obtained from density functional theory (DFT) simulations (Paper III).

Important to note is that the second expression is only valid for isotropic conditions. The result of this is that the elastic peaks get less defined with increasing temperature and also with increasing Q [165].

The MSD can be calculated from measurements of elastic fixed window scans (EFWSs), *i.e.* measurements of the elastic intensity as a function of temperature. The MSD generally shows a linear behaviour at low temperatures and as the vibrations of the material get activated at higher temperatures, the slope of the MSD increases (Fig. 3.5).

Phonons involve interaction in the (ideally) entire lattice of the material, therefore the part of the scattering function, $S(Q, \omega)$, that is of interest is the coherent part, $S_{\text{coh}}(Q, \omega)$. It can be shown that the intensity of the i th molecular phonon transition is proportional to

$$S_{\text{coh}}(Q, \omega_i) \propto I_i \propto Q^2 U_i^2 \exp(-Q^2 u_{\text{Total}}^2) \sigma, \quad (3.6)$$

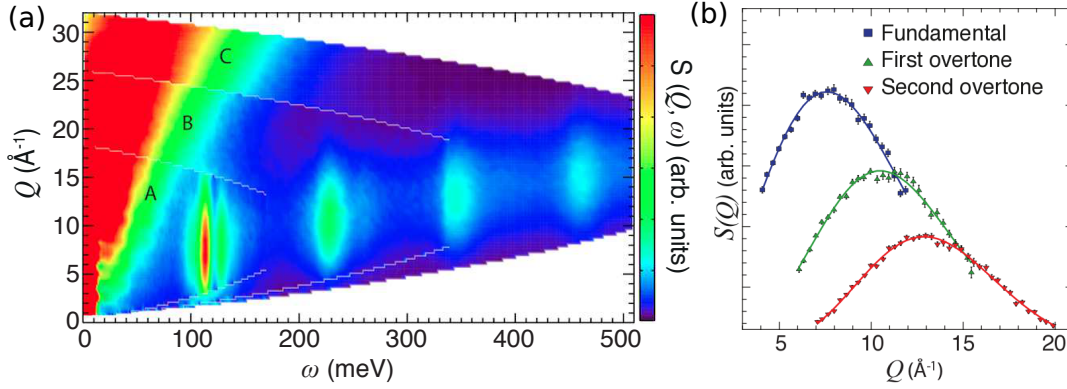


Figure 3.6: (a) INS intensity, $S(Q, \omega)$, for $\text{BaTiO}_{3-x}\text{H}_x$ (Paper III). The intensity is shown by colour coding. The Q -dependence can be obtained for the different modes by integrating over certain energy (ω) intervals. The Q -dependence together with the fitted line to the fundamental ($n=1$), first overtone ($n=2$) and second overtone ($n=3$) is shown in (b). The maximum of the curves occurs at higher Q -values when the order of the transition increases, which is in accordance to Eq. (A.8).

where ω_i is the i th mode at frequency ω and U_i is the amplitude of the phonon of the atom undergoing the particular mode [170]. The exponential term is again the Debye-Waller factor, with u_{Total} being the MSD of all the atoms in all the modes, both internal and external (explained in appendix A.1), and σ is the inelastic cross section of all the atoms involved in the mode. Hence, if there is no translational diffusion, the intensity decays as [171]

$$I(Q) \approx e^{-Q^2 \langle u^2 \rangle / 3}, \quad (3.7)$$

where $\langle u^2 \rangle$ is the MSD. The change of slope of the MSD that depends on the phonons in the material can be calculated from the INS spectra of the material. However, when the atomic mass becomes small enough, as for hydrogen, one can think of the vibrational motion as decoupled and localised from the rest of the lattice and the incoherent part of the INS spectrum needs to be considered. Hence, the incoherent approximation is used to develop a description of the dynamic response of the incoherent scattering from hydrogen atoms in a powder sample [172]. More specific, the INS intensity associated to the vibration of a specific atomic species l depends on the neutron scattering cross section σ_l and this is relatively large for hydrogen atoms (82.0) [173]. The INS intensity is

also affected by the amplitude of the vibrations, which is generally higher for lighter atoms. Consequently, the INS spectra of $\text{BaTiO}_{3-x}\text{H}_x$ should be mostly dominated by the motion of the hydride ions. The details of how to analyse the vibrational modes of the hydride ions, ν_{H} , and hence, how to derive the MSD values, is given in appendix A.1. A result of this is that the INS measurement (seen in Fig. 3.6) will thus provide the Q -dependence, which in turn can be used to study both the mean square dependence but also to distinguish between fundamental and higher-order transitions in the vibrational spectra [174–176].

3.4 Quasielastic neutron scattering

QENS refers to those scattering processes which are almost elastic (small loss or gain of energy) and show up as a broadening of the elastic peak (Fig. 3.7). Generally, the QENS is analysed by the fitting of a Lorentzian component, or several Lorentzians, describing the QENS peak, this to investigate the self-dynamics (diffusional motion) in the sample [177, 178]. Of specific interest in this thesis is to investigate the self-dynamics of hydrogen. Since hydrogen has a large incoherent cross section and a small coherent cross section, it is possible to separate the hydrogen motions from the rest of the material. The total dynamical scattering function can therefore be approximated with the incoherent one, *i.e.* $S(Q, \omega) \approx S_{\text{inc}}(Q, \omega)$.

The Q -dependence of the area [$A_i(Q)$] and the full width at half maximum [$\Gamma_i(Q)$] of the QENS peak is what is obtained in order to extract relevant results regarding the diffusional motion in the material. The measured scattering function, $S_{\text{meas}}(Q, \omega)$, is then used to extract this information and it can be modelled with

$$S_{\text{meas}}(Q, \omega) = S_{\text{inc}}(Q, \omega) \otimes R(Q, \omega), \quad (3.8)$$

where Q denotes the momentum transfer and ω is the energy transfer [136]. The instrumental resolution is represented by $R(Q, \omega)$ in the above equation. It is not uncommon to further add a background in the measured spectra corresponding to peak tails of fast atomic vibrations (INS) or too fast diffusional motions for the instrument to resolve properly. In the case of (pure) quasielastic

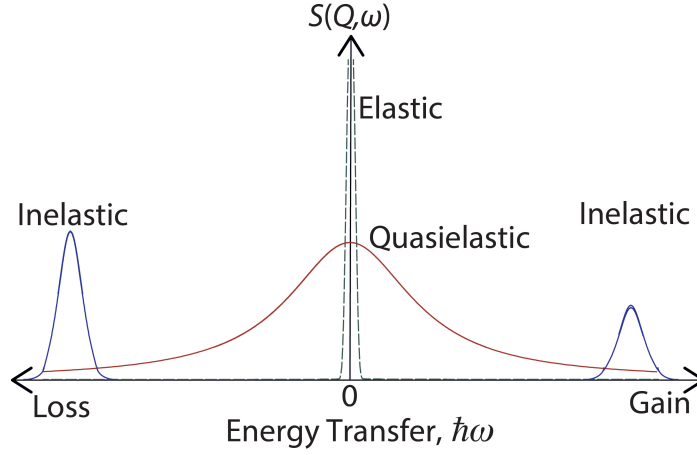


Figure 3.7: $S(Q, \omega)$ of a fixed Q -value, with a quasielastic peak, the elastic peak and the inelastic peaks further out from the zero energy transfer point ($\hbar\omega = 0$).

scattering, $S_{\text{inc}}(Q, \omega)$ may be expressed as

$$S_{\text{inc}}(Q, \omega) = A_0(Q)\delta(\omega) + \sum_i A_i(Q)L_i(Q, \omega). \quad (3.9)$$

In the equation above is the elastic peak represented by a delta function, $\delta(Q, \omega)$ and the $L_i(Q, \omega)$ s are Lorentzian functions describing the quasielastic peak. These Lorentzian functions are given by

$$L_i(Q, \omega) = \frac{2}{\pi} \frac{\Gamma_i(Q)}{(2\hbar\omega)^2 + \Gamma_i(Q)^2}. \quad (3.10)$$

Here, $\Gamma_i(Q)$ is the full width at half maximum (FWHM) of the Lorentzian, which relates to a characteristic relaxation time, also known as correlation time, τ_i , of the dynamics giving rise to quasielastic scattering, according to

$$\tau_i = \frac{2\hbar}{\Gamma_i}. \quad (3.11)$$

Hence, the Lorentzian functions, through $\Gamma_i(Q)$ and $A_i(Q)$, contain information about both the time-scale and Q -dependence of the observed dynamics. Additionally, the area, A_0 and A_i , of the QENS peak over Q can give information about the spatial characteristics of the dynamics, as will be described below.

3.4.1 Elastic incoherent structure factor

Since the QENS spectra are measured as a function of Q , the geometry of the observed localised motion(s) can be obtained from the ratio of the elastic (incoherent) scattering intensity $A_0(Q)$, [Eq. (3.9)] to the total (incoherent) scattering intensity, plotted as a function of Q . The total incoherent scattering intensity is the sum of the intensities of the elastic and quasielastic scattering and follows the assumption that the quasielastic and vibrational motions are separable, *i.e.* they occur on different time-scales. The resulting function is commonly referred to as the elastic incoherent structure factor (EISF),

$$\text{EISF} = \frac{A_0(Q)}{A_0(Q) + A_i(Q)}, \quad (3.12)$$

where $A_i(Q)$ denotes the area of the Lorentzian describing the quasielastic peak [134]. The EISF is unity at $Q = 0$ and falls to a minimum at a Q -value that relates to the spatial geometry of the dynamics. For instance, for a jump motion between three equivalent sites, the EISF is an oscillatory function of Q that approaches a minimum of $1/3$ at large values of Q , whereas a jump motion between four equivalent sites yields a different oscillatory EISF function that approaches a minimum of $1/4$ at large values of Q [179]. Therefore, higher- Q data are often required to distinguish between likely models describing the diffusional motion in order to observe this critical minimum. This criterion demands the use of higher-energy (shorter-wavelength) neutrons which however, will result in poorer energy resolution, a largely unavoidable characteristic of neutron spectrometers. By comparing the experimental EISF with geometrically feasible models, the geometry of motion can often be revealed. A general expression for the EISF (A_0) can be generated for N number of equivalent sites according to

$$A_0(Q) = \frac{1}{N} \sum_{n=1}^N j_0(Qr_n), \quad (3.13)$$

where j_0 is the zeroth-order spherical Bessel function [$j_0 = \sin(x)/(x)$] and r_n is the jump distance [177]. By comparing the experiment EISF with physically sound theoretical models, the geometry of the observed motion can often be realised.

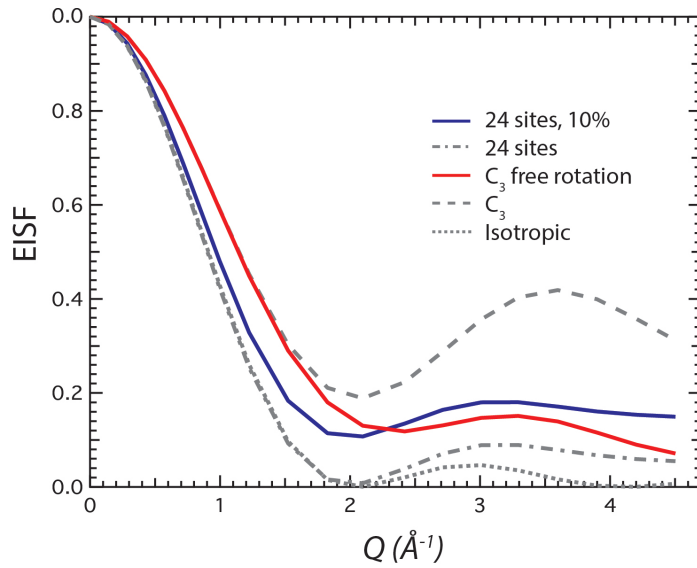


Figure 3.8: EISF models, corresponding to five distinct reorientational motions; free rotation about the C_3 axis (red), 24 hydrogen sites situated on a sphere with 10% of immobile hydrogen (blue), 3-site jumps around the C_3 axis (dashed line), and the isotropic rotational diffusion model where all positions around the Si atom is possible (dotted line). The dashed/dotted line is the same as the blue curve but with no immobile hydrogen.

The approach to analyse the EISF is to first evaluate the most likely model corresponding to the structure of the material, and then to fit the model to the EISF over Q . The following is the mathematical expressions for four different, in this thesis relevant, reorientational models, namely (i) 120° reorientations around a C_3 axis, (ii) free rotational motion around the C_3 axis, (iii) isotropic diffusional motion, and (iv) rotational diffusion around 24 sites. Fig. 3.8 shows the EISFs corresponding to these models. Considering first model (i), the C_3 axis rotations model is expressed as

$$\text{EISF}_{C_3} = \frac{1}{3}[1 + 2j_0(\sqrt{2}r_1Q)], \quad (3.14)$$

where r_1 is the jump distance calculated from the structure of the material investigate, alternatively this is quantity you gain from fitting this model to the EISF. Continuing to model (ii), the hydrogens perform free rotations around the C_3 axis (C_3 free rot.). A general formula is then easily realised where the

angle changes with the number of sites [179]

$$\text{EISF}_{\text{free rot.}} = \frac{1}{N} \sum_{n=1}^N j_0[2Qr \sin(\frac{n\pi}{N})]. \quad (3.15)$$

The curve will approach a specific shape and position as the N value increases. For $N \geq 50$, the rotational diffusion may be considered as free diffusion around a circle with radius r . In model (iii) the minimum of the EISF should approach 0, and hence represent the limiting case of isotropic rotational diffusion. The molecule is then free to reorient in any direction with small jump distances and the probability of the hydrogen positions is therefore anywhere on a sphere with the radius of r surrounding the center of mass atom

$$\text{EISF}_{\text{iso}} = j_0^2(Qr). \quad (3.16)$$

Model (iv) allows the hydrogen atoms to move between 24 different sites on a sphere, similar to model (iii) but with some predefined jump distances.

$$\text{EISF}_{24 \text{ sites}} = \frac{1}{24} [1 + j_0(Qd_1) + j_0(Qd_2) + \dots + j_0(Qd_{23})], \quad (3.17)$$

where the 23 jump distances (d_1, d_2, \dots, d_{23}) correspond to the 24 different hydrogen locations. If a fraction of the hydrogen atoms is immobile (the experiment did not reach high enough temperature or some of the hydrogen belongs to an impurity phase), one can simply add the relevant percentage to account for this. For example, if 10% of the hydrogens are immobile the following expression can be realised [180],

$$\text{EISF}_{24 \text{ sites}, 10\% \text{ immobile H}} = 0.9 \times \text{EISF}_{24 \text{ sites}} + 0.1. \quad (3.18)$$

In Fig. 3.8 the model in blue represents model (iv) with this addition of 10% immobile hydrogen atoms.

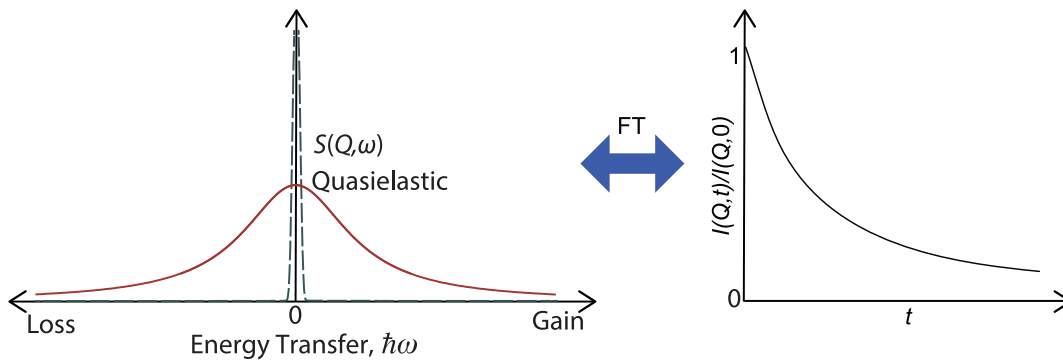


Figure 3.9: Schematic illustration of the quasielastic peak, $S(Q, \omega)$, which Fourier transforms into an exponential decay, that is the normalised intermediate scattering function, $I(Q, t)/I(Q, 0)$

3.5 Neutron Spin-Echo

Neutron spin-echo (NSE) refers to a special technique to do QENS measurements. It does not measure the scattering function $S(Q, \omega)$ but instead the intermediate scattering function $I(Q, t)$, hence the time dependence of the dynamical motion is probed directly [181]. Fourier Transformation (FT) is used to convert $S(Q, \omega)$ into $I(Q, t)$, thus, if $S(Q, \omega)$ is a Lorentzian line, then the FT will be an exponential decay (Fig. 3.9). What the NSE instruments then measure is the normalised intermediate scattering function, $I(Q, t)/I(Q, 0)$ [181]. A simplified explanation of the spin-echo techniques is that you look at how long (t) an atom stays within a specific distance (Q) before it diffuses out of the measured length. The normalised intermediate scattering function is then how big of a fraction of atoms that will participate in that specific diffusional length and time.

A special feature of the NSE technique, is that it enables the separation of coherent and incoherent scattering. Specifically, this is possible due to the spin-incoherent scattering has a probability of $2/3$ to change the spin state of the neutron [182, 183]. This can be exploited for, *e.g.*, the determination of hydrogen content in a material at different temperatures.

4

Instrumentation

4.1 Neutron sources and the production of neutrons

There are two main types of neutron sources, the spallation source, where the neutrons are generated by colliding accelerated charged particles into a heavy element (target), and the reactor source, where neutrons are produced through nuclear fission. A key difference between the two is that with a spallation source the neutrons are produced in pulses as the particles hit the target material, whereas in a reactor source, the neutrons are produced continuously [165]. Initially, the neutrons will have a high velocity/energy, but are then slowed down by the help of a moderator, which will yield neutrons with distinct ranges of energies/wavelengths suitable for the different instruments [165]. In this thesis, I have used nine different instruments, at both reactor and spallation sources; three inelastic spectrometers (TOSCA, MERLIN and VISION), four quasielastic spectrometers (DCS, IN16B, BASIS and HFBS), one spin-echo spectrometer (NSE), and one diffractometer (D20). A concise description about the key aspects of each instrument is given in the following.

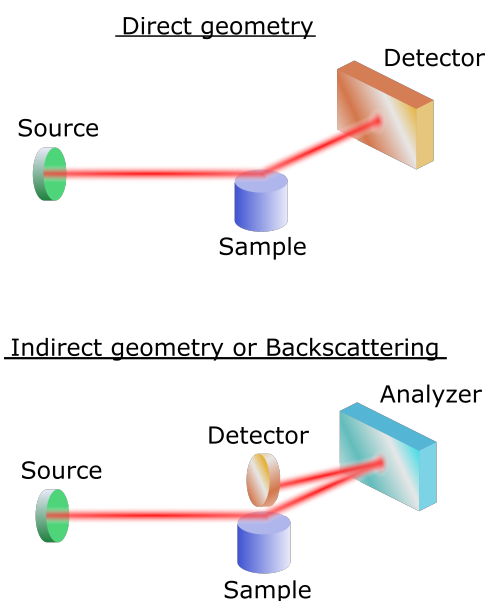


Figure 4.1: Schematic drawing of the direct geometry (upper) and indirect geometry/backscattering (lower) that neutron spectrometers can exhibit.

4.2 Inelastic spectrometers

The TOSCA, VISION and MERLIN spectrometers were used for the study of the local environment of hydride ions in $\text{BaTiO}_{3-x}\text{H}_x$. TOSCA and MERLIN [184–187] are inelastic neutron spectrometers optimised for the determination of vibrational spectra of materials. Both are situated at the ISIS neutron and muon source at the STFC Rutherford Appleton Laboratory, Chilton, Didcot, Oxfordshire, UK. The two instruments work complementary to each other. TOSCA covers a wide range from 0 to 8000 cm^{-1} of the vibrational spectrum in a single measurement and the samples under investigation may in addition be mounted on a multi-sample-changer. Hence, TOSCA enables fast and continuous measurements with high resolution. The resolution of the MERLIN instrument [186, 187] is lower compared to TOSCA, but MERLIN offers the possibility to record the full $S(Q, \omega)$ map, where one gets both the momentum ($Q, \text{Å}^{-1}$) and energy transfer (ω, meV) independently. TOSCA is an indirect geometry time-of-flight spectrometer (Fig. 4.1), where the time-of-flight technique is used for energy analysis of the scattered neutrons, hence the final energy is a known, fixed value. MERLIN is instead a direct geometry spectrometer where the incident energy is at a fixed value [188].

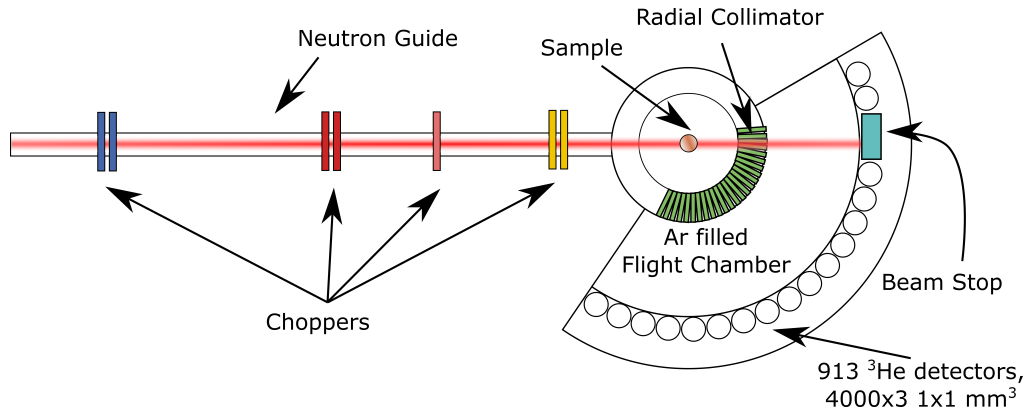


Figure 4.2: Schematic drawing of the DCS instrument, exhibiting a direct geometry.

VISON is situated at the Spallation Neutron Source (SNS) at the Oak Ridge National Laboratory in USA [189] and shares many characteristics with TOSCA. VISON has a similar resolution as TOSCA and it also follows a fixed trajectory in (Q, ω) space, *i.e.* there is a single momentum transfer (Q) associated with each energy transfer (ω). VISON was used on a complementary basis to TOSCA for the INS measurements in this thesis.

INS instruments measure vibrations on the femto seconds to picosecond time scale, but in order to detect diffusional motion in the picosecond time scale one needs a time-of-flight quasielastic spectrometer, such as the Disc Chopper Spectrometer (DCS), as described below.

4.3 Quasielastic spectrometers

4.3.1 The Disc Chopper Spectrometer

The DCS [190] at the NIST Center for Neutron Research (NCNR), Gaithersburg (USA), is a direct geometry time-of-flight instrument (Fig. 4.2), which can detect rapid diffusional motion, and was used in this thesis to study the localised diffusion in the alkali silanides, $ASiH_3$ ($A = K, Rb$). DCS uses neutrons with wavelengths in the range ~ 2.3 to ~ 10 Å, which are selected by a monochromating chopper system (Fig. 4.2) [191]. The determination of the energy exchange, during the scattering event, is then based on the measurement

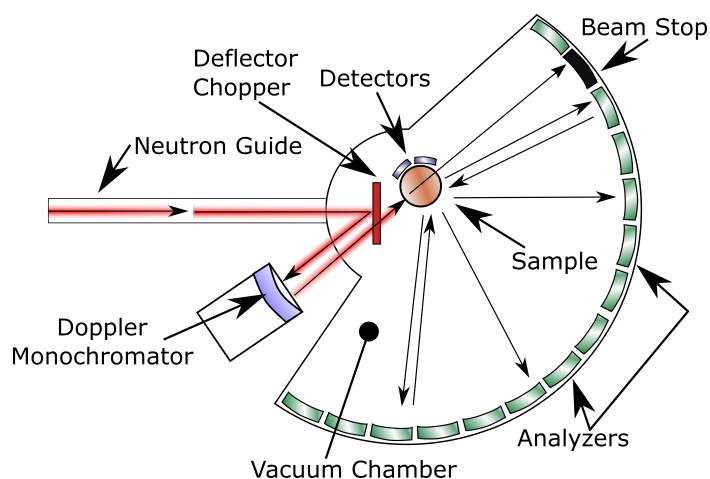


Figure 4.3: Schematic drawing of a backscattering spectrometer.

of the time-of-flight before and after scattering. This is done with a chopper system, based on a set of rotating discs, that turns the beam into pulses, which enables the time-of-flight to be measured. With the use of 2.5 \AA neutrons, the energy resolution and accessible Q -range of the spectrometer are $745 \mu\text{eV}$ at FWHM, and $0.98\text{--}4.48 \text{ \AA}^{-1}$, respectively. The accessible relaxation times are (hence) of the order $\sim 0.01 \text{ ps}$ to $\sim 1 \text{ ps}$. The energy resolution increases and the Q -range is reduced when using longer wavelengths. The slowest dynamics that can be probed by DCS are characterised by time-scales of the order of 100 ps . To measure even slower time scale dynamics, such as long-range diffusion, one may use a backscattering spectrometer.

4.3.2 Backscattering spectrometers

A backscattering spectrometer exhibits a higher resolution than a time-of-flight instrument and is therefore suited for studies of much slower processes, such as long-range diffusion. In this thesis, backscattering spectrometers were used for measuring the long-range diffusional motion of the hydride ions in $\text{BaTiO}_{3-x}\text{H}_x$ at different temperature intervals. The monochromization of the incoming neutron beam and the energy analysis of the scattered neutrons are achieved by Bragg diffraction on single-crystals at a backscattering instrument (Fig. 4.3). In this context, the wavelength spread, $\delta\lambda$, of a Bragg-diffracted neutron beam

decreases as the scattering angle, 2θ , approaches 180° , according to [192];

$$\frac{\delta\lambda}{\lambda} = \frac{\delta d}{d} + \frac{\delta\theta}{\tan\theta}. \quad (4.1)$$

Hence, if the neutrons are scattered 180° (backscattering), that is θ approaches 90° , the term containing the angle vanishes. The only term then left to influence the wavelength divergence is the d -spacing term. Therefore, by choosing a material for the single-crystal with an appropriate spread in spacing, one can influence the beam convergence significantly. Silicon (111) plane is the one most commonly used, with a $\frac{\delta d}{d}$ of 1.86×10^{-5} . With this configuration the beam will become more monochromatic and give a better resolution. The backscattering spectrometers used in this thesis were the HFBS at NCNR [192, 193], IN16B at ILL [194, 195], and BASIS at SNS [196].

HFBS exhibits a good resolution of $0.83 \mu\text{eV}$ of the FWHM, but a rather limited dynamical range of ≈ 20 ps to 2 ns. The Q range of HFBS is 0.6 to 1.6 \AA^{-1} , which is rather similar for all three instruments (0.1 to 1.8 \AA^{-1} for IN16B and 0.2 to 2 \AA^{-1} for BASIS). HFBS is suitable for EFWSs measurements, which are particularly useful for determining the temperature at which the dynamics are accessible to the instrument.

IN16B is rather similar to the HFBS instrument (a resolution of $0.75 \mu\text{eV}$ at FWHM, a dynamical range of ≈ 20 ps to 2 ns, and enables EFWSs to be measured), but due to a slightly different configuration, IN16B exhibits less background noise and higher flux ($6.0 \times 10^5 \text{ n/cm}^2/\text{s}$ for IN16B and $3 \times 10^5 \text{ n/cm}^2/\text{s}$ for HFBS).

BASIS exhibits a lower resolution of $3.5 \mu\text{eV}$ at FWHM compared to HFBS and IN16B, but instead BASIS gives access to a larger dynamic range of ≈ 2 ps to 0.1 ns. In addition, due to BASIS being situated at a spallation source, the instrument displays a significantly higher flux of $1.3 \times 10^7 \text{ n/cm}^2/\text{s}$ compared to HFBS and IN16B, which will enable shorter measuring times.

To measure even longer time scales than what is possible with a backscattering instrument, one needs to take advantage of a different QENS technique, the neutron spin-echo (NSE) technique.

4.3.3 Neutron spin-echo

The NSE instrument at the NCNR [197, 198] was used for detecting a loss of hydride ions in $\text{BaTiO}_{3-x}\text{H}_x$ at a certain temperature in connection to an onset of diffusional motion. The NSE instrument makes it possible to measure the highest resolution possible at sub μeV over a wide range of incident wavelengths [181, 183]. This gives the possibility to observe extremely slow processes, at the far end up to 200 ns, but also fairly fast at 3 ps. A quite wide Q -range is assessable, from 0.02 to 1.8 \AA^{-1} , depending on the chosen wavelength. The great resolution of the NSE technique comes from the utilisation of polarising the spin of the neutrons ($S = 1/2$). This is exploited to encode the difference in energies between the incident and the scattered beam. The details of how the NSE instrument works is given in appendix B.1.

Important to note is that because of the incoherent scattering exhibits a $1/3$ reduced echo amplitude, it is more difficult to measure QENS of small sample amount or materials with a low density of hydrogen [181], such as the $\text{BaTiO}_{3-x}\text{H}_x$ material as studied in this thesis.

4.4 Neutron diffractometer

The neutron diffraction measurements in this thesis were performed on the D20 instrument at ILL [199, 200] and was used for measuring the lattice parameter of ReO_3 as a function of temperature. The D20 diffractometer is featured by a two-axis diffractometer capable of producing a very high intensity of neutrons at the sample position. This paves the way for swift measurements with high amount of counts and therefore it is often possible to do real-time and temperature dependent measurements, for example, to follow structural phase-transitions in real time.

The great advantage of neutron diffraction (compared to X-ray diffraction), is the possibility to observe hydrogen atoms, thanks to the large neutron scattering cross section of hydrogen atoms. This gives the opportunity to indirect observe hydrogen atoms as a large background (due to the diffuse scattering, hence incoherent scattering) which will show the conjunction between structural change over temperature and the presence of hydrogen spices. This is of

great important for the relationships between dynamics and structures in this thesis.

5

Results

5.1 Local structure and dynamics of perovskite type oxyhydrides

The perovskite type oxyhydrides, $\text{BaTiO}_{3-x}\text{H}_x$, were investigated with the aim to determine the dynamical behaviour of the hydride ions by using QENS (Paper I). Measurements of EFWSs suggested not only the presence of vibrational motions but also the presence of diffusional motions of the hydride ion (Fig. 5.1). In particular, the diffusional hydride ion dynamics were investigated at "low temperatures", 225 and 250 K, and revealed dynamics on the time-scale of nanoseconds and at "high temperatures", 400, 500, 600 and 700 K, which revealed dynamics on the time-scale of picoseconds. Specifically, the Q -dependence of the quasielastic widths showed a long-range diffusional behaviour with a jump length of 2.8 Å at low temperatures, corresponding to a nearest neighbour jump. At high temperatures, the jump length increased to 4 Å, which was interpreted as second nearest neighbour jumps, see Fig. 5.1. A complementary study by our colleagues in Stockholm [69] showed that the studied materials contained a considerable amount of oxygen vacancies (stated in Paper I), which may significantly enhance the diffusivity of the hydride ions. In fact, a small oxygen vacancy concentration effect can be seen in the materials, as the sample with the highest oxygen vacancy concentration shows generally shorter residence times. This is in full accordance to previous investigations

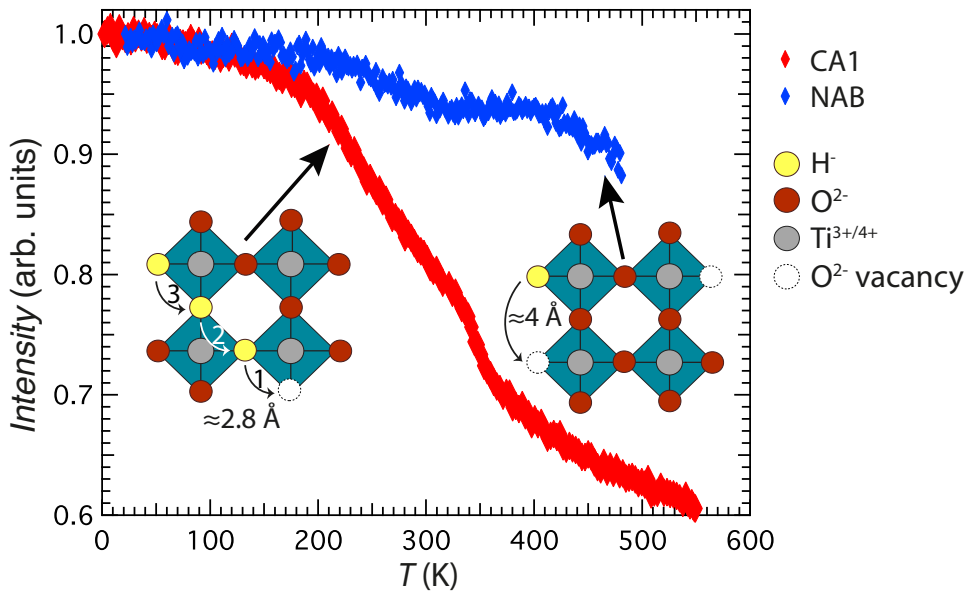


Figure 5.1: Normalised EFWSs of CA1 and NAB, as measured on IN16B and HFBS, respectively, together with the schematic illustration of the observed hydride-ion dynamics corresponding to nearest neighbour jumps (left) at low (≤ 250 K) and second nearest neighbour jumps (right) at high (> 400 K) temperatures.

[77, 109], where the hydride diffusional motion in for example EuTiO_3 has been significantly enhanced by introducing oxygen vacancies in the material. The observed activation energy of the hydride ion diffusion in $\text{BaTiO}_{3-x}\text{H}_x$ is rather low, 0.1 eV, but similar to what has been observed in a previous QENS study of hydride ion diffusion in the oxyhydride $\text{LaSrCoO}_3\text{H}_{0.7}$, which exhibited an activation energy of 0.2 eV [108]. However, these values of activation energies are inconsistent with a recent study of the diffusivity of the hydride ion by a deuterium exchange, where an activation energy of 2 eV was reported [101]. Important to note is that the two investigational techniques probe different type of diffusional motion. QENS measures the pure bulk self-diffusion of the hydride ion, whereas deuterium exchange measures the entire conductivity and is regulated by the chemical potential between the gas and solid phase. Furthermore, a spin-echo measurement was conducted, in order to further confirm the effects of introducing oxygen vacancies on the hydride ion diffusivity. A decrease of the incoherent scattering (the hydride ion concentration) was detected at 595 K, which coincided with a small decay of $I(Q, t)/I(Q, 0)$, hence showing

the correlation between hydrogen loss (creating oxygen vacancies) and the onset of diffusional motion in the sample. These results are of importance when designing future ion conducting materials, showing that a small concentration of vacancies can change the ion conductivity in the material.

Building on these exciting results, I turned to investigate the position(s) and local environment of the hydride-ions by using INS. This was done in close collaboration with theoreticians that used calculations based on DFT to determine the vibrational spectra of $\text{BaTiO}_{3-x}\text{H}_x$ (Paper II). Crucially, we demonstrated that the hydride-ion is located at the oxygen site and not as covalently bonded to the oxygens, as for example in proton conducting equivalents such as $\text{BaTi}_{1-x}\text{Y}_x\text{O}_3\text{H}_x$. Furthermore, we showed that the electrons form a bandstate configuration and not a polaron. The formation of a polaron, where the electron localises on a titanium ion, causes a local lattice distortion. This affects the hydride ion vibrational modes (Fig. 5.2) and introduces a big chemical expansion (calculated by DFT). Electrons delocalised in the bandstate show less chemical expansion (DFT) and hence corresponds more closely to the values measured by INS and the reported values by Kobayashi *et al.* [68]. However, the electronic configuration in $\text{BaTiO}_{3-x}\text{H}_x$ has previously been attributed to the polaronic state [96], which would explain the observed blue colour of the material [86]. Nonetheless, this is in sharp contrast to the studies on thin films of $\text{ATiO}_{3-x}\text{H}_x$ ($A = \text{Ba}, \text{Sr}, \text{Ca}$), which report a high electronic conductivity [30, 79]. The combination of INS and DFT calculations confirm that the electrons in bulk $\text{BaTiO}_{3-x}\text{H}_x$ form a bandstate configuration. This implies that the material exhibits metallic conductivity.

We also performed several additional INS experiments on the same samples as in Paper I, with the aim to elucidate more about the localisation of the Ti-H vibrations and the defect chemistry of the samples (Paper III). The results from INS, in agreement with DFT calculations, showed the presence of Ti-H vibrational modes at 114 and 128 meV (Fig. 5.3). Additionally, the MSD of the Ti-H vibrations in $\text{BaTiO}_{3-x}\text{H}_x$ was extracted from the INS data and shows close to no change over temperature. This is in full accordance with our DFT calculations of the material, proving that these modes are highly localised. The structure does not only include hydride ions but also oxygen vacancies, which significantly influences the local environment around the hydride ion. Addi-

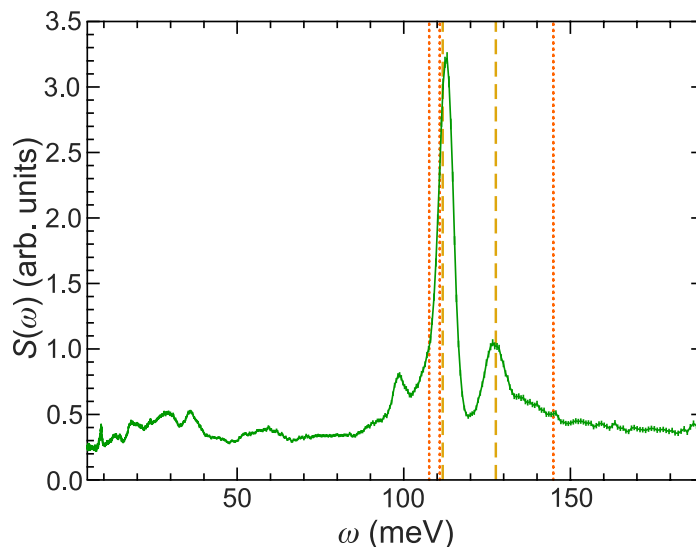


Figure 5.2: INS spectra at $T < 10$ K of CA2 recorded on TOSCA. The dotted orange line is the calculated position of the polaron configuration and the dashed yellow line is the calculated position of the bandstate configuration (Paper II).

tional peaks were observed in close proximity of the two main Ti-H vibrational modes and showed a broadening with increasing oxygen vacancy concentration. This has previously been observed for both SrTiO_{3-x} and BaTiO_{3-x} , hence in materials containing oxygen vacancies. DFT calculations confirmed that the additional vibrational peak at 100 meV (Fig. 5.3) stem from a local configuration with an oxygen vacancy as the nearest neighbour to the hydride ion. This proves the existence of oxygen vacancies, positioned as the nearest neighbour to the hydride ion, which then is contributing to diffusional motion even at low temperature (Paper I).

Finally, in order to pursue complementary fundamental knowledge about the local environment of hydrogen species in a perovskite structure, I studied a hydrogen-containing sample of the perovskite type oxide ReO_3 (Paper IV). This material is significantly simpler than the oxyhydride material due to the vacant A-site structure and would therefore reduce the number of competing contributions to the local environment and dynamics. ReO_3 is therefore a highly interesting material and is an optimum prototype perovskite material to study. In particular, the NTE of the lattice parameter [Fig. 5.4 (a)] was investigated by the means of NPD and complementary TGA measurements.

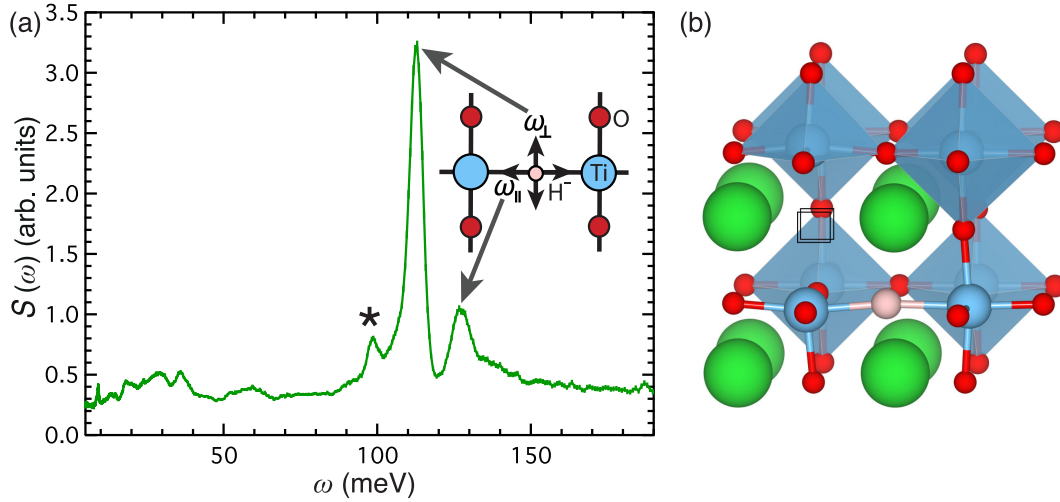


Figure 5.3: (a) INS spectra at $T < 10$ K of CA2 recorded on TOSCA together with a sketch indicating the direction of ω_{\parallel} and ω_{\perp} Ti-H vibrational motions in $\text{BaTiO}_{3-x}\text{H}_x$. The grey arrows indicate which vibrational mode corresponds to which peak. (b) An illustration of the configuration containing both a hydride ion (pink) and an oxygen vacancy defect (square) contributing to the small peak indicated by the black star.

Interestingly, the results show conflicting results between that of the polycrystalline powder sample (COMM) compared to the single crystal sample (SC). The COMM sample displayed a large background in the NPD measurement [Fig. 5.4 (b)], originating from the incoherent scattering associated with hydrogen species, while the SC sample showed a much reduced background [Fig. 5.4 (b)], indicating the absence of hydrogen species. Furthermore, for the COMM sample, the TGA and NPD show a broad loss of hydrogen species from 300 K to 425 K, which is not to be related to surface water as it affected the lattice parameter.

The main difference between the COMM sample and the SC sample is then hypothesised to be a certain amount of oxygen vacancies present in the COMM sample, but absent in the fully stoichiometric SC sample. The implication of our TGA and NPD results is that each cycle of drying or vacuum treatment on the ReO_3 samples will increase the number of oxygen vacancies and change the observed NTE behaviour. Oxygen vacancies control the size and range of the NTE as the vibrational breathing mode of the ReO_6 octahedra controls the NTE, and which would be impacted by oxygen vacancies. NPD measurements

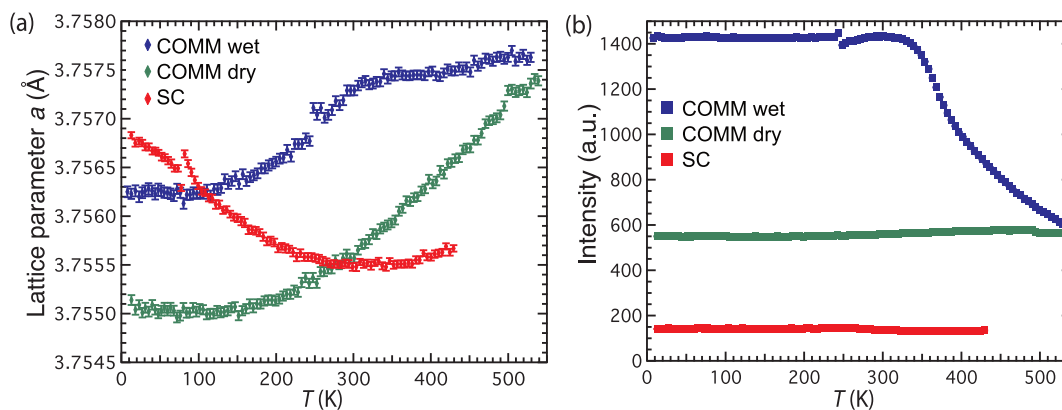


Figure 5.4: (a) Lattice parameter and (b) background over temperature for the two samples of ReO_3 , COMM (dry and wet) and SC, as measured on D20.

show that the material is cubic throughout the measured temperature range, with no peak broadening indicative of the orthorhombic distortion as previously reported by Weller [83–85] for the bronzes (H_xReO_3). Furthermore, the residual gas analyser connected to the TGA only detected water (as of hydrogen origin) during the mass loss steps, implying that the hydrogen species in the sample are not hydride ions (would leave as H_2), but rather of some combination of oxygen and hydrogen. We interpret this as the hydrogen species present in the material is water molecules intercalated into the vacant A -site of the perovskite structure. The incorporation of the water molecules is mediated by low levels of oxygen vacancies in the perovskite lattice. An increase in oxygen vacancies results in a more moisture sensitive material. The presence of hydrogen bonds from the intercalated water to the oxygen framework further disrupts the ReO_6 breathing mode, leading to a suppression of the NTE.

The sum of these results is highly important, because it tells the story about the hydrogen species in the perovskite structure from a before untold viewpoint. Thus, expanding the knowledge about solid oxide materials, functioning both as ion and proton conductors. The hydride ions perturb the perovskite lattice in a significant way, not like a vacancy and not like a proton but rather like an atomic substitution, giving the material new characteristics. The material is no longer changing structure over temperature but keeps the cubic structure, and a long-range diffusion can be measured at lower temperature due to the presence of oxygen vacancies in a combination with the hydride ions. Furthermore,

the hydrogen species in ReO_3 is mediated through oxygen vacancy diffusion, which both influences phonon modes of the material and changes the minima of the NTE. This, and the knowledge above related to hydrogen species and oxygen vacancies, will likely help when designing and developing new materials for technical applications such as proton conducting fuel cells and hydride ion conducting batteries.

5.2 Localised hydrogen diffusion in alkali silanides

In the area of hydrogen storage materials, I have focused my research on the investigation of hydrogen dynamics in KSiH_3 and RbSiH_3 , using QENS (Paper V). As introduced in Chapter 2.3.3, these materials are unique in that they exhibit absorption/desorption of hydrogen within a good pressure and temperature window for fuel cell applications. In more detail, the QENS studies were separated into measurements of both above and at the order-disorder phase transition temperature occurring at around 270–305 K.

Measurements upon heating showed the onset of strong quasielastic scattering around the phase-transition temperature demonstrating that the phase-transition is dynamical in nature (Fig. 5.5). In order to describe the dynamics, the previously reported structure of a quasi-spherical arrangement with 24 sites of preferred orientations for the hydrogen atoms around each Si atom (determined on the basis of neutron diffraction data [48]) was used as a starting point in the analysis of the quasielastic data. In somewhat more detail, a re-orientation model was considered, that do not necessarily preserve a particular orientation of the SiH_3^- ions in the NaCl-type crystal structure, but in fact describes a jump diffusion on the surface of a sphere, with 24 different jump locations (Fig. 5.6). The 24 different jump locations are derived from the SiH_3^- molecule being confined inside a cubic lattice, where the hydrogen atoms do not entirely fit in the corner, but the positions of the hydrogen will instead be distorted. For every corner position this would generate three hydrogen positions and therefore lead to a total number of 24 positions on a sphere around the Si atom close to the corners of the cube (Fig. 5.6). The 24 sites model represents

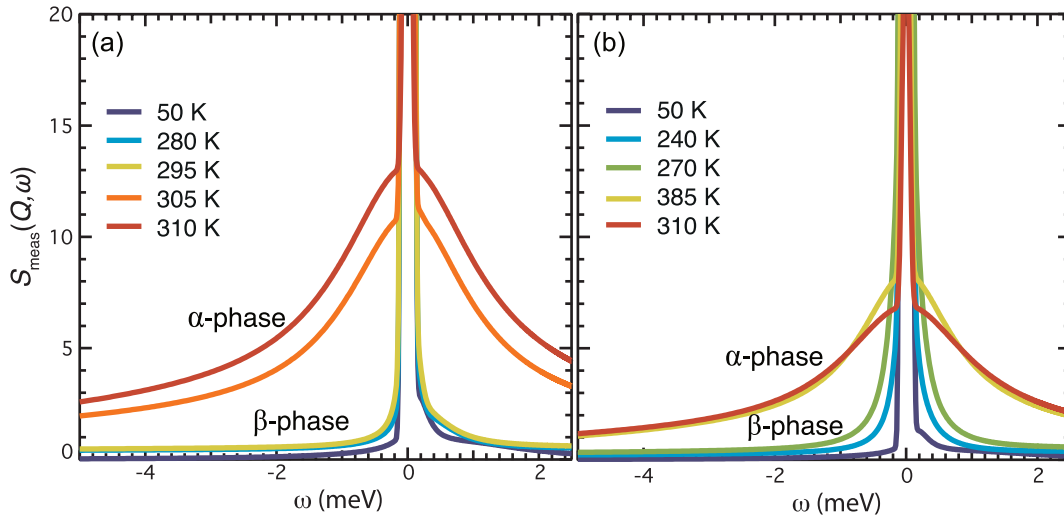


Figure 5.5: The fit to the QENS spectra when increasing the temperature for (a) KSiH_3 and for (b) RbSiH_3 at $Q = 1.9 \text{ \AA}^{-1}$, measured with 4.8 \AA neutrons on the DCS instrument. A significant increase of the QENS peak intensity is observed when going from the β - to the α -phase.

thus a combination of a rotational diffusion motion and a localized jump model. The model is similar to the isotropic rotational diffusion model, but with the difference that it includes small jump distances to preferred hydrogen sites. Additionally, to get a satisfactory and physically sound fit, a constant of 0.1 (10%) was added to the model, in order to account for scattering of H atoms that do not contribute to the observed dynamics. A suggested explanation for the missing 10% of quasielastic scattering was that some diffusional information was lost in the background subtraction of the analysis, due to difficulties to achieve a complete separate extraction of the background. The background probably stems from; i) vibrational motions, ii) the very fast diffusional motion, or iii) continuous rotational diffusion on a circle around the eight C_3 axes.

The average relaxation time between successive jumps is of the order of sub-picoseconds and exhibits a weak temperature dependence with a small difference in activation energy between the two materials, $39(1) \text{ meV}$ for KSiH_3 and $33(1) \text{ meV}$ for RbSiH_3 .

Recently, Tang *et al.* [157] complemented our results of the α -phase dynamics in KSiH_3 and RbSiH_3 by adding an extensive report on CsSiH_3 . The SiH_3^- reorientational dynamics for α - CsSiH_3 was measured on the same instrument

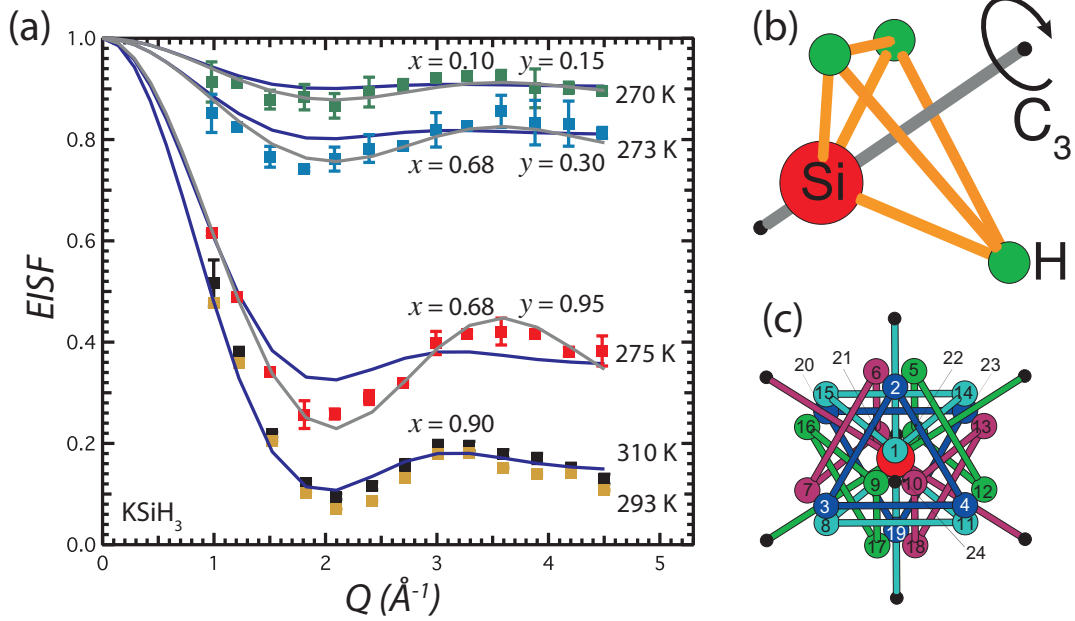


Figure 5.6: EISF during cooling over the phase transition for KSiH_3 from data obtained using 2.5 \AA neutrons (a). Two models are presented: the C3 model (b) [grey line in (a)] and the 24 sites model (c) [blue line in (a)]. The fractions of mobile hydrogen, contributing to an offset for the C3 model and the 24 sites model, are shown by the values of y and x , respectively in (a).

(DCS) and showed the same type of dynamics (the 24 sites model), solidifying and confirming our results. The reported activation energy for $\alpha\text{-CsSiH}_3$ [32(3) meV] was similar to our results for $\alpha\text{-KSiH}_3$ [39(1) meV] and $\alpha\text{-RbSiH}_3$ [33(1) meV], but showed a small decrease in reorientational mobilities with the increasing size of the cation, hence the high-temperature disordered α -phase is dependent on the cation environment.

In the same paper, Tang *et al.* [157] extended the study to also include results from EFWSs of the same materials (KSiH_3 , RbSiH_3 and CsSiH_3) over the phase transitions. A big intensity drop of the elastic peak was observed with EFWS measurements at 75–80 K for CsSiH_3 , 150 K for RbSiH_3 , and 225 K for KSiH_3 . This suggests an onset of dynamical hydrogen motion visible for the HFBS instrument (detecting dynamics in the dynamical time scale of ≈ 20 ps to 2 ns) at those specific temperatures [157]. The temperature difference shows a cationic radii dependence, where the material with the smallest cation, KSiH_3 , exhibits the highest temperature, hence the SiH_3^- ion in this material

has the most difficulties to reorientate [157, 201]. At even higher temperatures, the quasielastic component becomes too broad (the motion becomes too fast) for the instrument to detect and the EFWSs *vs.* temperature becomes flat. This flattening coincides with the phase transfer from the β - to the α -phase, hence the reorientational motion in the α -phase is significantly more rapid [157]. However, there is a small second plateau observed at temperatures just below the phase transition, for CsSiH₃ and RbSiH₃. Tang *et al.* [157] explained this as a more restricted SiH₃⁻ ion reorientational mechanism before the material completely turns into the α -phase. Furthermore, when cooling the materials back to the β -phase, a hysteretic, compound-dependent, rise of the EFWS intensities were observed, similar to the previously mentioned differential thermal analysis, indicating that the dynamical behaviour of the materials, influences or follows the phase transitions.

Little was still known about the actual phase transition, how this rigid solid structure actually turns into a highly dynamic material at a certain temperature. I therefore studied the order-disorder phase transition in the same two alkali silanides, RbSiH₃ and KSiH₃ (Paper VI). Several techniques were used to investigate the materials; NPD, Raman spectroscopy, heat capacity, solid-state ²H NMR spectroscopy, and QENS. QENS measurements upon heating show that the phase transition occurs at 279 and 300 K for RbSiH₃ and KSiH₃ (Fig. 5.5), respectively. In order to describe the dynamics observed in QENS, the previously reported 24 sites jump model was used as a starting point at high temperatures that then turn into a C₃ model at the phase transition (Fig. 5.6). The reorientational mobility of H atoms in undercooled α -phase is reduced, with relaxation times on the order of picoseconds. The occurrence of rotator phases in α -ASiH₃ near room temperature and the presence of dynamical disorder even in the low-temperature β -phases imply that SiH₃⁻ ions are only weakly coordinated in an environment of A⁺ cations. Therefore, the phase transition is not an abrupt step but rather a gradual process, which could be something to strive for in materials when looking for new or enhanced materials for hydrogen storage.

Most recently, a continuation of my phase transition study was performed on the HFBS instrument by Dimitrievska *et al.* [202], in order to catch the slow dynamics of the low temperature β -phase. Measurements were conducted

when increasing the temperatures (going from β - to α -phase) to increase the temperature interval where the β -phase dynamics could be observed before the phase transition [202]. Indeed, the observed jump model follows the structure of the β -phase and show a 120° three-site jump model around the 3-fold symmetry axis (the C_3 model) of the SiH_3^- ion. When reaching the α -phase, the dynamical motion becomes faster and the QENS peak moves out of the window of the HFBS instrument. However, this dynamical phase transition, seems not to be abrupt, but rather shows an undercooled α -phase during the transition [158]. It has also been hypothesised that this undercooled dynamical phase transition is actually an intermediate phase, the i -phase, which shows a dynamical model somewhere in between the 120° three-site jump model and the more rapid disordered model at high temperatures. This model would then include diffusional rotations around the 3-fold symmetry axis of the SiH_3^- ion, with no preference for the 3 jump sites observed in the β -phase. However, the i -phase has yet to be confirmed with diffraction studies or the like, and also to be observed not only in CsSiH_3 but likewise in RbSiH_3 and KSiH_3 [202].

In summary, my results, in combination with more recent results, show that the SiH_3^- ions are in a close to gaseous phase but still in a solid material, with a phase transition that slowly freezes rather than abruptly changes. Besides being of considerable fundamental interest, the better understanding of the nature of SiH_3^- reorientational mobility in the disordered phases of KSiH_3 and RbSiH_3 could explain the low entropy variation for hydrogen absorption/desorption and hence the origin of these materials' favourable hydrogen-storage properties. Thus, as the material is similar to a free gas but with the advantage of not needing to pressurise/depressurise the gas itself, it presents a great advantage and thus simplifying the refuelling of a car.

6

Conclusions and outlook

To conclude, this thesis provides new important fundamental knowledge about the local structure and dynamics in perovskite oxyhydrides and alkali silanides. In particular, it is found that the hydride ion dynamics in $\text{BaTiO}_{3-x}\text{H}_x$ is featured by long-range diffusion composed of a nearest neighbour jump at low temperatures (225 and 250 K) and a second nearest jump at high temperatures (400, 500, 600, 700 K). The diffusional motion was promoted by the relatively high oxygen vacancy concentration present in the material. Additionally, the vibrational motion of the hydride-ions, was investigated both experimentally and with DFT calculations, which showed that the hydride-ions were indeed located on vacant oxygen sites. It was further confirmed that the extra electron, originating from the hydride ion configuration, form a delocalized bandstate. This study is an excellent example of how the combination of first-principles calculations and INS experiments is a particular appropriate tool for studying the vibrational motion of the hydride ions. Furthermore on this note, both experimental and theoretical calculations confirmed the existence of a local environment where an oxygen vacancy is the nearest neighbour to the hydride ion, in agreement with the nearest neighbour jumps of the long-range diffusion. In the related compound ReO_3 , a clear hydrogen species and vacancy dependence on the negative lattice thermal expansion was observed. The hydrogen specie in the material is in the form of intercalated water molecules, mediated by low levels of oxygen vacancies in the perovskite lattice. This shows the versatility of the perovskite structure, able to accommodate both protons, hydride ions

but also whole water molecules.

Looking towards the future, there are lots of possibilities to extend the presented studies. A concrete sequel to the results of this thesis could be to investigate the localised and long-range diffusion of H^- atoms in $\text{ATiO}_{3-x}\text{H}_x$ and how it depends on both the A -site atom ($A = \text{Ca}, \text{Sr}$ and Ba) and on the hydride ion concentration (x), with the aim to elucidate how the A -site atom influences the diffusional path and vibrational frequencies. Furthermore, a most interesting study to conduct would be to investigate with QENS the dynamical behaviour and conduction of the hydride-ions in $\text{BaTiO}_{3-x}\text{H}_x$ synthesised as a film and how this depends on x , with the purpose to investigate the hydride-ion dynamics in a material more similar to the electrolyte material in a fuel cell. This will enable conductivity studies together with the effect of strain in the material and how it influences the diffusion of hydride-ions. In addition to the continuation of the study on $\text{BaTiO}_{3-x}\text{H}_x$, further measurements (INS and QENS) need to be conducted on the hydrogen containing ReO_3 material with different hydration levels to elucidate how the hydrogen content influences the local structure and if any diffusional motion can be detected. The aim of this study would be to create a prototype perovskite material containing both protons and hydride ions, and hence a material most relevant for bridging the results between proton conducting materials and oxyhydrides.

A project that is already initiated, is the study of how the structure of the host material influences the hydride ion diffusional motion. QENS and INS measurements have been conducted on SrVO_2H , which adopts a perfectly ordered, tetragonal, structure, containing V^{3+} [203]. Here, each V^{3+} is coordinated by four O^{2-} in a square planar fashion and two trans-oriented H^- complete the octahedral coordination. Many of the cubic structured oxyhydrides have disordered anionic distributions, although SrVO_2H is an exception due to the local bonding preferences [67]. Preliminary results can be seen in Fig. 6.1, where QENS data at 300 K [Fig. 6.1(a)] have been fitted similar to the data analysis of the QENS measurements on $\text{BaTiO}_{3-x}\text{H}_x$. The FWHM ($\Gamma_1(Q)$) over Q for SrVO_2H at 300 K [Fig. 6.1(a)] exhibits a similar shape as for $\text{BaTiO}_{3-x}\text{H}_x$ at 400 K. Specifically, the data fitted with a Chudley-Elliot model reveals a jump distance of 2.7 Å, hence in close proximity of the nearest neighbour distance (≈ 2.7 Å) in tetragonal SrVO_2H [203]. However, as SrVO_2H

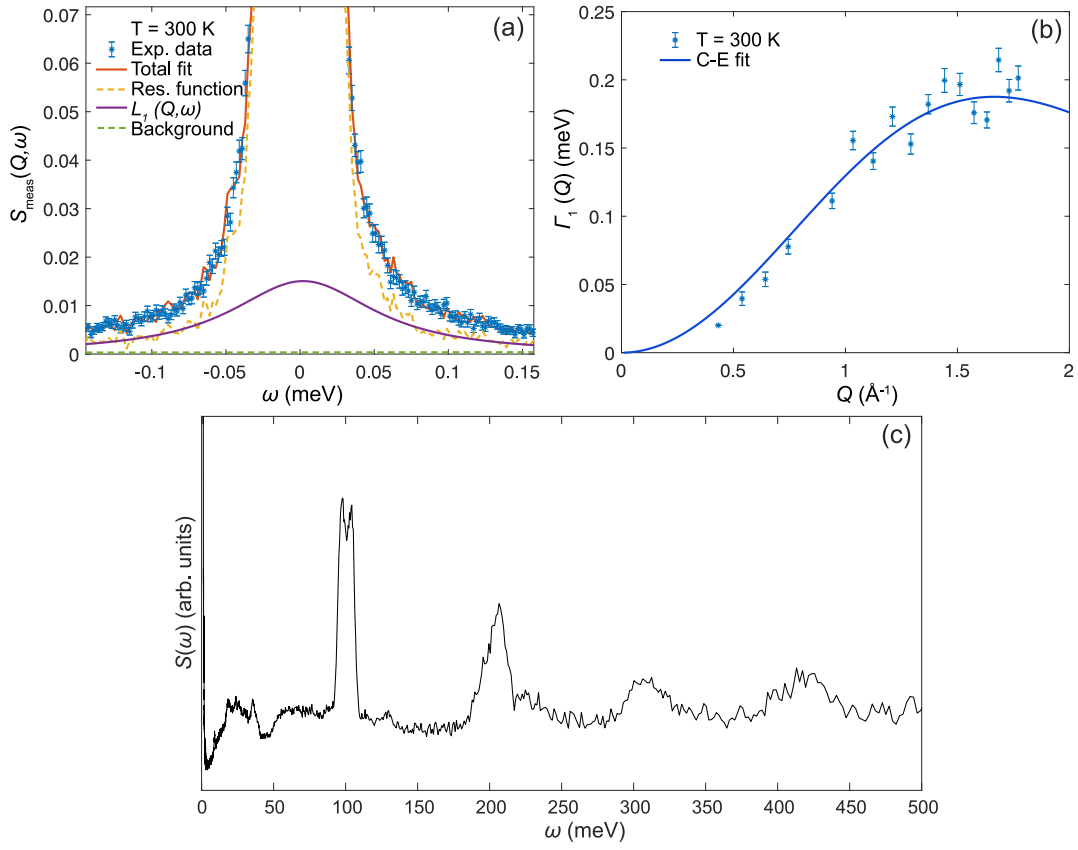


Figure 6.1: (a) $S_{\text{meas}}(Q, \omega)$ of SrVO_2H at $Q = 1.73 \text{ \AA}^{-1}$ and 300 K, as measured on OSIRIS, together with the best fit. (b) $\Gamma_1(Q)$ of SrVO_2H , as extracted from the OSIRIS data at 300 K. The solid lines are fits to a Chudley-Elliott model. (c) INS spectra at $T < 12 \text{ K}$ of SrVO_2H recorded on TOSCA.

is a fully ordered material, the nearest neighbour to the hydride ion position is not occupied by a hydride ion but rather an oxygen atom. One can only assume that this position might instead be vacant and that the oxygen vacancy concentration in the SrVO_2H would stimulate a hydride ion diffusional motion. This needs to be further investigated through a careful fit of the INS spectrum of SrVO_2H [Fig. 6.1(c)], preferably in combination with DFT calculations, similar to the approach in Paper III. Hence, a local environment of the hydride ion dominated by oxygen vacancies could in that case be identified.

With regard to the alkali silanides, it has been shown that the localised diffusional behaviour of hydrogen atoms exhibits jump diffusion on the surface of a sphere with 24 different jump locations. Investigations of the dynamical behaviour over the phase transition (from α - to β -phase) revealed how

the dynamical motions begin to "freeze in" and the slower C_3 axis rotations starts to dominate. A continuation of this work could be to investigate similar materials in order to further elucidate how the structure of the material influences the hydrogenation/dehydrogenation behaviour and how the localised diffusion changes with the structure type. A reasonable structure to investigate, which would further increase the hydrogen gravimetric storage density, would be LiSiH_4 . This material would give a unique insight of the influence of the A -site atom on the dynamical motion. Unfortunately, this compound has not yet been synthesised but only been predicted by first principles calculations [204]. Another opportunity to study the influence of the A -site atom on the dynamical properties would be to investigate the hydrogen dynamics in $A\text{BeH}_3$ [205, 206] or $A\text{MgH}_3$ [207] ($A = \text{K, Rb, Cs}$). However, also these compounds have only been predicted and characterised with first principles calculations, but would work as a bridge between our QENS study of the alkali silanides and another recent QENS study of the super lightweight compound LiBeH_3 [208]. The LiBeH_3 compound shows great promise when it comes to hydrogen gravimetric storage density but the synthesis process is rather complicated and hydrogenation/dehydrogenation have not fully been investigated. A highly interesting and relevant study to conduct would be to investigate the dynamics in the high-pressure structure of the $\text{SiH}_4(\text{H}_2)_2$ complex [209]. This would give a direct view of the pure SiH_4 dynamics, presumably similar to the dynamics of the SiH_3^- ion. The $\text{SiH}_4(\text{H}_2)_2$ complex would serve as a most interesting hydrogen storage material and will probably be subjected to extensive investigations in the near future.

On a more technical note, future advances of neutron scattering instruments will enable shorter measurements with higher precision, which will allow even more detailed and extensive studies of hydrogen containing materials. In addition to this, and of special interest to research groups within Sweden, is that we have the construction of the ESS (European Spallation Source) just on our doorstep in Lund [210]. The ESS will generate up to 100 times more neutrons than similar facilities, which will enable shorter measuring times and the possibility to increase the statistics. This is of significant importance when studying hydride ion dynamics in oxyhydride materials, as the QENS peak, according to my experience, tend to be small and otherwise difficult to resolve.

A

Inelastic neutron scattering details

A.1 MSD derived from the Q -dependence

The following section will in more detail analyse the vibrational modes, ν_{H} , of the hydride ions.

The vibrational mode of the hydride ion (ν_{H}) can be described by its vibrational energy ω_{ν} and the displacement vector $\mathbf{u}_{\text{H},\nu}$ along the direction of the vibration. From ref [172, 176] we get the intensity associated to this mode (turn to Ref. [172] to get the complete derivation and Refs. [211, 212] to get a more general derivation) which is expressed as

$$S'(\mathbf{Q}, \omega_{\nu})_{\text{H}}^{(n)} \propto \frac{(\mathbf{Q} \cdot \mathbf{u}_{\text{H},\nu})^{2n}}{n!} \exp \left[- \left(\mathbf{Q} \cdot \sum_{\nu} \mathbf{u}_{\text{H},\nu} \right)^2 \right], \quad (\text{A.1})$$

where $S'(\mathbf{Q}, \omega_{\nu})_{\text{H}}^{(n)}$ is the measured scattering intensity, and the sum denotes that it runs over all the vibrational modes of the hydrogen atom. The n value denotes a fundamental mode or some of the overtones, hence $n = 1$ are fundamental modes, $n = 2$ their first overtones, $n = 3$ their second overtones, and so forth. An overtone is a single quantum effect, that is an excitation of a higher-order transition. This differs from multiple scattering phenomena that involve two (or more) scattering events separated in space and time. There

is also the possibility to simultaneously excite two different vibrational modes resulting in a combination of bands, which again is a single quantum effect.

Furthermore, the derivation of Eq. (A.1) is based on three assumptions; i) all modes are dynamically separated from each other (decoupled), as previously mentioned ii) the scattering is described as completely incoherent and, iii) $2k_B T/\hbar\omega \ll 1$, hence the high energy modes of the hydride ions is basically temperature independent. Additionally, the INS intensity is given by the average of Eq. (A.1) taken with respect to all possible directions of \mathbf{Q} , [172, 176] as the analysis here concerns a powder sample where the crystals are oriented in all direction, *i.e.*

$$S(Q, \omega_\nu) = \frac{1}{4\pi} \int S'(\mathbf{Q}, \omega_\nu) d\mathbf{Q}. \quad (\text{A.2})$$

This expression can be simplified by using the *almost isotropic oscillator approximation*. This approximation is valid for the vibrational modes of the hydride ions in BaTiO₃ due to the possibility to assume that the displacements in the different vibrational modes ν_H are all similar to the average value of $u_{\text{H,int}}^2/3$, *i.e.*

$$|\mathbf{u}_{\text{H},\nu}|^2 \approx \frac{1}{3} u_{\text{H,int}}^2 = \frac{1}{3} \sum_{\nu=1}^3 |\mathbf{u}_{\text{H},\nu}|^2 \quad \forall \nu. \quad (\text{A.3})$$

In this expression $u_{\text{H,int}}^2$ is the internal MSD, that is the highly localised vibrational modes of the Ti-H vibrations (usually located at higher energy above 90 meV). The intensity of the fundamental bands for these internal modes can be expressed (using the *almost isotropic oscillator approximation*) as [172, 175]

$$S(Q, \omega_\nu)_H = Q^2 \gamma_{\text{H},\nu}^{(1)} e^{-Q^2 \alpha_{\text{H},\nu}^{(1)}} \quad (\text{A.4})$$

where

$$\gamma_{\text{H},\nu}^{(1)} \propto u_{\text{H},\nu}^2, \quad \alpha_{\text{H},\nu}^{(1)} = \frac{1}{5} (u_{\text{H,tot}}^2 + 2u_{\text{H},\nu}^2), \quad (\text{A.5a})$$

$$u_{\text{H,tot}}^2 = u_{\text{H,int}}^2 + u_{\text{H,ext}}^2. \quad (\text{A.5b})$$

Here $u_{\text{H},\nu}^2$ stands for the scalar quantity $|\mathbf{u}_{\text{H},\nu}|^2$, $u_{\text{H,tot}}^2$ is the total MSD of

a hydride ion. Furthermore, the external contribution to the MSD, that is the lattice modes (phonons, usually located at lower energy), is represented by $u_{\text{H,ext}}^2$. Indicated by the equation above is that this new coefficient, γ , is dependent on the mean square displacement, however it is also proportional to the intensity of the INS band. To further include a description of the overtones and combinational modes, one can generalise Eq. (A.4) by

$$S(Q, \omega)_{\text{H}}^{(n)} = Q^{2n} \gamma_{\text{H}}^{(n)} e^{-Q^2 \alpha_{\text{H}}^{(n)}}, \quad (\text{A.6})$$

where $n = 1$ for the fundamental modes, $\omega = \omega_{\nu}$ and the coefficients $\gamma_{\text{H}}^{(1)}$ and $\alpha_{\text{H}}^{(1)}$ are defined in Eq.(A.5a). First order of overtones will on the other hand be represented by $n = 2$, $\omega = 2\omega_{\nu}$ and binary combination modes in relation to this will be represented by $n = 2$, $\omega = \omega_{\nu} + \omega_{\nu'}$. Whereas the coefficients α_{H} and γ_{H} are given by the following expressions

$$\gamma_{\text{H},\nu}^{(2)} \propto u_{\text{H},\nu}^4, \quad (\text{A.7a})$$

$$\alpha_{\text{H},\nu}^{(2)} = \frac{1}{7} (u_{\text{H,tot}}^2 + 4u_{\text{H},\nu}^2), \quad (\text{A.7b})$$

$$\gamma_{\text{H,comb}}^{(2)} \propto u_{\text{H},\nu}^2 u_{\text{H},\nu'}^2, \quad (\text{A.7c})$$

$$\alpha_{\text{H,comb}}^{(2)} = \frac{1}{7} (u_{\text{H,tot}}^2 + 2u_{\text{H},\nu}^2 + 2u_{\text{H},\nu'}^2). \quad (\text{A.7d})$$

The maximum of $S(Q, \omega)_{\text{H}}^{(n)}$ can be derived from differentiation of Eq. (A.6) and occurs when

$$Q = Q_{\text{max}}^{(n)} = \sqrt{n/\alpha_{\text{H}}^{(n)}}. \quad (\text{A.8})$$

Then to apply the almost isotropic oscillator approximation, and assuming $u_{\text{H,ext}}^2$ to be negligible, the following will be obtained

$$\alpha_{\text{H},\nu}^{(1)} \approx \alpha_{\text{H},\nu}^{(2)} \approx \alpha_{\text{H,comb}}^{(2)} \approx u_{\text{H,int}}^2/3,$$

which leads to

$$Q_{\text{max}}^{(n)} \approx \sqrt{n} Q_{\text{max}}^{(1)}. \quad (\text{A.9})$$

Subsequently, by fitting the Q -dependence one can obtain both the value of γ_{H} and of α_{H} , and hence derive the MSD values.

B

Neutron spin-echo details

B.1 Operation principle

When the neutrons approach the NSE instrument, they first go through a velocity selector [Fig. B.1(b)], this to narrow the spread of the velocity of the neutrons to 10-20% and hence increase the resolution of the instrument [183, 213]. In the second step, the neutrons go through a polariser that align all spins in the direction of the velocity, followed by a $\pi/2$ flipper [Fig. B.1(a)], which changes the spin to be perpendicular to the magnetic field produced by the coils of the instrument [181, 213]. This starts the precession where the neutrons experience a torque from a magnetic field B perpendicular to its spin direction [214], hence

$$N = S \times B. \quad (\text{B.1})$$

This together with the gyromagnetic ratio of $\gamma = g_n \mu_N / \hbar$ (where g_n is the g-factor of the nucleus and μ_N is the nuclear magneon) gives the precession with the Larmor frequency,

$$\omega_L = \gamma B, \quad (\text{B.2})$$

that the neutron makes in the magnetic field [Fig. B.1(c)] [183]. Faster neutrons will spend less time in the first precession coil and hence have a smaller precession angle (the opposite is true for slower neutrons) [213]. At the π flipper, the neutrons are not only flipped 180° but the phase are inverted. After the π flipper the neutrons will go through the sample and interact, hence exchange

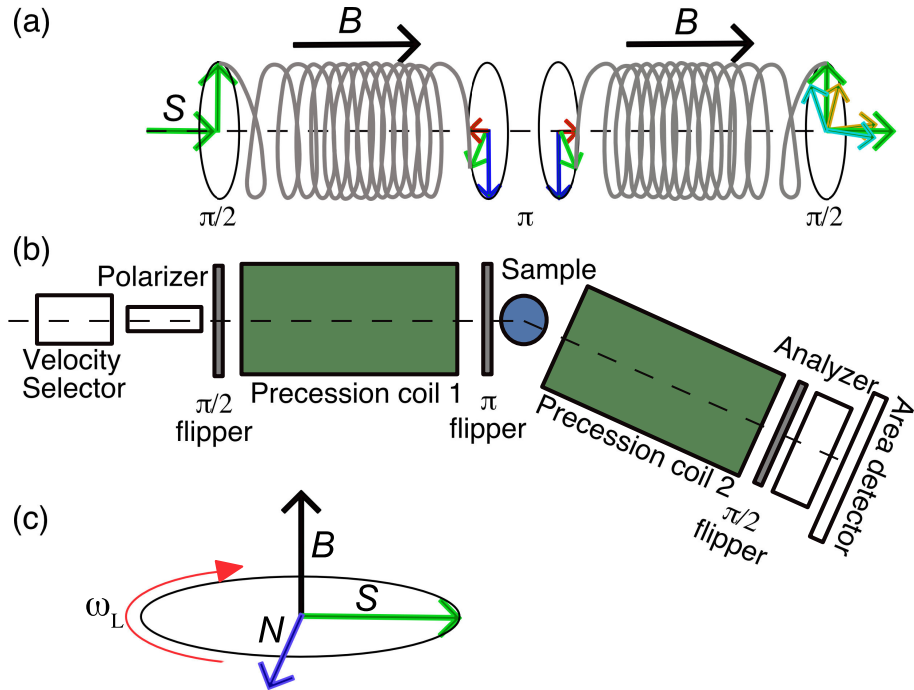


Figure B.1: (a) Simplified schematic figure of the spin-echo technique. Green arrows are the spin of the neutron, red arrows are fast neutrons and blue arrows are slow neutrons. Teal and orange arrows are inelastic scattered neutrons. (b) A schematic figure of a Spin-Echo instrument. (c) How the precession of the neutron's spin behaves in an applied magnetic field, where S is the spin of the neutron, B is the magnetic field, N is torque experienced by the neutron perpendicular to its spin.

momentum and energy (velocity). In the second precession coil, the neutrons that did not exchange momentum and energy, will precess all the way back to their initial angle and at the second $\pi/2$ flipper they will once again stop the precession and align the spin in the direction of the velocity [181]. However, the neutrons that did interact with the sample will have a changed angle and thus the polarisation of the scattered neutron beam will be proportional to the intermediate scattering function at a specific value of t . The specific value of t will be determined by the strength of the precession field (and by the incident neutron wavelength).

Acknowledgements

I would first like to thank my supervisor Maths for his readiness and support, the fast feedback and for giving me the opportunity to do my PhD at Chalmers. Thanks to my colleagues Laura, Daria, Yuan-Chih, and Erik, for helping me with my projects and also for your vital friendships. Thanks to my former office mates, Andrea and Martin, for all the non-scientific conversations and for teaching me some Italian words. Thanks to my co-supervisor Göran for the inspiring scientific discussions, Reji, Ulrich, and his group in Stockholm, for synthesising the materials and the great scientific inputs, Paul Henry for his enthusiasm, Aleks for being my first examiner, Sten for being my second examiner, Ezio for his support in the lab and to all my colleagues at both KMF and OOMK for the great support and all the interesting lunch chats. I would further like to thank all the local contacts at NIST, ILL and ISIS, especially Antonio and Madhu for your hospitality and the great discussions about neutron scattering, Stewart for the help with measuring and interpreting the INS data, and Bernhard for sharing your immense knowledge with me.

I would finally like to thank all my friends and family. My deepest gratitude and love to my parents, Marie and Thomas, for your encouragement when it is needed the most, for teaching me about minerals and meteorites, and your endless support. A lot of love and thanks to my brother Eric for always challenging me and for cheering me up. And at the very last, my humble and greatest gratitude to Johnas, my husband and best friend. You are the gravity that keeps me centered and the person that can always make me smile. You fill my life with warmth, interesting discussions and the most delicious food there is to find. But you have also given me the greatest gift of all, Folke. I love you both to the infinity and beyond.

Carin

Bibliography

- [1] UNTC, *The Paris Agreement*, XXVII 7.d, 2015-12-12.
- [2] J. Rogelj, M. Den Elzen, N. Höhne, T. Fransen, H. Fekete, H. Winkler, R. Schaeffer, F. Sha, K. Riahi and M. Meinshausen, *Nature*, 2016, **534**, 631–639.
- [3] O. Ellabban, H. Abu-Rub and F. Blaabjerg, *Renewable and Sustainable Energy Reviews*, 2014, **39**, 748–764.
- [4] R. F. Service, *This new fuel cell could turbocharge renewable power*, Science, 2018-02-12.
- [5] M. Shaner, S. Davis, N. Lewis and K. Caldeira, *Energy and Environmental Science*, 2018, **11**, 914–925.
- [6] N. Belmonte, C. Luetto, S. Staulo, P. Rizzi and M. Baricco, *Challenges*, 2017, **8**, 1–15.
- [7] K. Møller, T. Jensen, E. Akiba and H.-W. Li, *Progress in Natural Science: Materials International*, 2017, **27**, 34–40.
- [8] C. Liu, F. Li, M. Lai-Peng and H.-M. Cheng, *Advanced Materials*, 2010, **22**, E28–E62.
- [9] H. Liu, A. Almansoori, M. Fowler and A. Elkamel, *International Journal of Hydrogen Energy*, 2012, **37**, 8905–8916.
- [10] J. Ren, S. Gao, S. Tan, L. Dong, A. Scipioni and A. Mazzi, *Renewable and Sustainable Energy Reviews*, 2015, **41**, 1217–1229.

-
- [11] M. Stygar and T. Brylewski, *International Journal of Hydrogen Energy*, 2013, **38**, 1–9.
- [12] M. Pudukudy, Z. Yaakob, M. Mohammad, B. Narayanan and K. Sopian, *Renewable and Sustainable Energy Reviews*, 2014, **30**, 743–757.
- [13] E. Wachsman and K. Lee, *Science*, 2011, **334**, 935–939.
- [14] E. Wachsman, T. Ishihara and J. Kilner, *MRS Bulletin*, 2014, **39**, 773–779.
- [15] L. Malavasi, C. A. J. Fisher and M. S. Islam, *Chem. Soc. Rev.*, 2010, **39**, 4370–4387.
- [16] D. Brett, A. Atkinson, N. Brandon and S. Skinner, *Chemical Society Reviews*, 2008, **37**, 1568–1578.
- [17] M. Peña and J. Fierro, *Chemical Reviews*, 2001, **101**, 1981–2017.
- [18] M. Karlsson, *Dalton Transactions*, 2013, **42**, 317–329.
- [19] M. Karlsson, *Phys. Chem. Chem. Phys.*, 2015, **17**, 26–38.
- [20] S. Choi, C. Kucharczyk, Y. Liang, X. Zhang, I. Takeuchi, H.-I. Ji and S. Haile, *Nature Energy*, 2018, **3**, 202–210.
- [21] L. Bi, S. Boulfrad and E. Traversa, *Solid State Ionics*, 2015, **275**, 101–105.
- [22] S. Hossain, A. Abdalla, S. Jamain, J. Zaini and A. Azad, *Renewable and Sustainable Energy Reviews*, 2017, **79**, 750–764.
- [23] L. Schlapbach and A. Züttel, *Nature*, 2001, **414**, 353–358.
- [24] H. Larsen, R. Feidenhans'l and L. Sønderberg Petersen, *Risø energy report 3. Hydrogen and its competitors*, 2004.
- [25] G. Kobayashi, Y. Hinuma, S. Matsuoka, A. Watanabe, M. Iqbal, M. Hirayama, M. Yonemura, T. Kamiyama, I. Tanaka and R. Kanno, *Science*, 2016, **351**, 1314–1317.

- [26] X. Liu, T. Bjørheim and R. Haugrud, *Journal of Materials Chemistry A*, 2018, **6**, 1454–1461.
- [27] M. Verbraeken, C. Cheung, E. Suard and J. Irvine, *Nature Materials*, 2015, **14**, 95–100.
- [28] X. Zhang, X. Wang, Q. Wang, X. Ma, C. Liu, P. Li, C. Liu, Y. Han, Y. Ma and C. Gao, *Physical Chemistry Chemical Physics*, 2018, **20**, 8917–8923.
- [29] T. Sakaguchi, Y. Kobayashi, T. Yajima, M. Ohkura, C. Tassel, F. Takeiri, S. Mitsuoka, H. Ohkubo, T. Yamamoto, J. Kim, N. Tsuji, A. Fujihara, Y. Matsushita, J. Hester, M. Avdeev, K. Ohoyama and H. Kageyama, *Inorganic Chemistry*, 2012, **51**, 11371–11376.
- [30] T. Yajima, A. Kitada, Y. Kobayashi, T. Sakaguchi, G. Bouilly, S. Kasahara, T. Terashima, M. Takano and H. Kageyama, *Journal of the American Chemical Society*, 2012, **134**, 8782–8785.
- [31] N. Masuda, Y. Kobayashi, O. Hernandez, T. Bataille, S. Paofai, H. Suzuki, C. Ritter, N. Ichijo, Y. Noda, K. Takegoshi, C. Tassel, T. Yamamoto and H. Kageyama, *Journal of the American Chemical Society*, 2015, **137**, 15315–15321.
- [32] Y. Kobayashi, O. Hernandez, C. Tassel and H. Kageyama, *Science and Technology of Advanced Materials*, 2017, **18**, 905–918.
- [33] D. Walter, A. Fell, Y. Wu, T. Duong, C. Barugkin, N. Wu, T. White and K. Weber, *Journal of Physical Chemistry C*, 2018, **122**, 11270–11281.
- [34] J. Mizusaki, K. Arai and K. Fueki, *Solid State Ionics*, 1983, **11**, 203–211.
- [35] P. Cheeseman and C. Angell, *Solid State Ionics*, 1981, **5**, 597–599.
- [36] S. Kim, N. Toyama, H. Oguchi, T. Sato, S. Takagi, T. Ikeshoji and S.-i. Orimo, *Chemistry of Materials*, 2018, **30**, 386–391.
- [37] R. Martínez-Coronado, A. Aguadero, D. Pérez-Coll, L. Troncoso, J. Alonso and M. Fernández-Díaz, *International Journal of Hydrogen Energy*, 2012, **37**, 18310–18318.

- [38] US Department of Energy, *Hydrogen Storage*, <https://www.energy.gov/eere/fuelcells/hydrogen-storage>, accessed 2019-02-24.
- [39] U. Eberle, M. Felderhoff and F. Schüth, *Angew. Chem.*, 2009, **48**, 6608–6630.
- [40] Toyota Motor Corporation, *FCV Fuel Cell Vehicle*, <http://www.toyota-global.com/innovation/>, accessed 2019-02-24.
- [41] A. Ramirez-Cuesta, M. Jones and W. David, *Materials Today*, 2009, **12**, 54–61.
- [42] N. de Miguel, R. O. Cebolla, B. Acosta, P. Moretto, F. Harskamp and C. Bonato, *International Journal of Hydrogen Energy*, 2015, **40**, 6449 – 6458.
- [43] R. Hirotani, T. Terada, Y. Tamura, H. Mitsuishi and S. Watanabe, *Thermal Behavior in Hydrogen Storage Tank for Fuel Cell Vehicle on Fast Filling.*, Society of Automotive Engineers Technical Report 2007-01-0688, 2007.
- [44] J.-N. Chotard, W. S. Tang, P. Raybaud and R. Janot, *Chem. Eur. J.*, 2011, **17**, 12302–12309.
- [45] A. Züttel, *Materials for Hydrogen Storage*, 2009, pp. 107–169.
- [46] D. Smith, *Fuelling the future: solid phase hydrogen storage*, <https://eic.rsc.org/feature/fuelling-the-future-solid-phase-hydrogen-storage/2020153.article>, accessed: 2019-02-24.
- [47] W. Tang, J. Chotard, P. Raybaud and R. Janot, *J. Phys. Chem. C*, 2014, **118**, 3409–3419.
- [48] V. Kranak, Y.-C. Lin, M. Karlsson, J. Mink, S. Norberg and U. Häussermann, *Inorganic Chemistry*, 2015, **54**, 2300–2309.
- [49] C. Sylwan and O. Lindström, *Nationalencyklopedin, bränslecell.*, <http://www.ne.se/uppslagsverk/encyklopedi/lång/bränslecell>, accessed 2019-02-24.

- [50] K. D. Kreuer, *Annu. Rev. Mater. Res.*, 2003, **33**, 333–359.
- [51] F. A. de Bruijn, V. A. T. Dam and G. J. M. Janssen, *Fuel cells 08*, 2008, **1**, 3–22.
- [52] D. E. Lehmann, *Neutron Imaging for Cultural Heritage Investigations*, <https://www.psi.ch/niag/cultural-heritage>, accessed 2019-02-24.
- [53] S. S. Zumdahl, *Hydride*, <https://www.britannica.com/science/hydride>, accessed: 2019-02-24.
- [54] F. Poulsen, *Solid State Ionics*, 2001, **145**, 387–397.
- [55] T. Arani, *Hydrides*, <https://chem.libretexts.org/>, accessed: 2019-02-24.
- [56] J. Mao, Z. Guo, X. Yu and H. Liu, *Journal of Physical Chemistry C*, 2011, **115**, 9283–9290.
- [57] P. Li, Z. Li, F. Zhai, Q. Wan, X. Li, X. Qu and A. Volinsky, *Journal of Physical Chemistry C*, 2013, **117**, 25917–25925.
- [58] K. Anderson and W. S. Fleshman, *Industrial & Engineering Chemistry*, 1950, **42**, 1381–1383.
- [59] M. Hayward, E. Cussen, J. Claridge, M. Bieringer, M. Rosseinsky, C. Kiely, S. Blundell, I. Marshall and F. Pratt, *Science*, 2002, **295**, 1882–1884.
- [60] B. Malaman and J. Brice, *Journal of Solid State Chemistry*, 1984, **53**, 44–54.
- [61] N. Clark and E. Wu, *Journal of The Less-Common Metals*, 1988, **142**, 145–154.
- [62] B. Huang and J. Corbett, *Inorganic Chemistry*, 1998, **37**, 1892–1899.
- [63] B. Huang and J. Corbett, *Journal of Solid State Chemistry*, 1998, **141**, 570–575.
- [64] P. Delporte, F. Meunier, C. Pham-Huu, P. Vennegues, M. Ledoux and J. Guille, *Catalysis Today*, 1995, **23**, 251–267.

- [65] V. Fokin, Y. Malov, E. Fokina, S. Troitskaya and S. Shilkin, *International Journal of Hydrogen Energy*, 1995, **20**, 387–389.
- [66] K. Hayashi, S. Matsuishi, T. Kamiya, M. Hirano and H. Hosono, *Nature*, 2002, **419**, 462–465.
- [67] Y. Kobayashi, Y. Tsujimoto and H. Kageyama, *Annual Review of Materials Research*, 2018, **48**, 303–326.
- [68] Y. Kobayashi, O. Hernandez, T. Sakaguchi, T. Yajima, T. Roisnel, Y. Tsujimoto, M. Morita, Y. Noda, Y. Mogami, A. Kitada, M. Ohkura, S. Hosokawa, Z. Li, K. Hayashi, Y. Kusano, J. Kim, N. Tsuji, A. Fujiwara, Y. Matsushita, K. Yoshimura, K. Takegoshi, M. Inoue, M. Takano and H. Kageyama, *Nature Materials*, 2012, **11**, 507–511.
- [69] R. Nedumkandathil, A. Jaworski, J. Grins, D. Bernin, M. Karlsson, C. Eklöf-Österberg, A. Neagu, C.-W. Tai, A. Pell and U. Häussermann, *ACS Omega*, 2018, **3**, 11426–11438.
- [70] Y. Goto, C. Tassel, Y. Noda, O. Hernandez, C. Pickard, M. Green, H. Sakaebe, N. Taguchi, Y. Uchimoto, Y. Kobayashi and H. Kageyama, *Inorganic Chemistry*, 2017, **56**, 4840–4845.
- [71] F. Denis Romero, A. Leach, J. Möller, F. Foronda, S. Blundell and M. Hayward, *Angewandte Chemie - International Edition*, 2014, **53**, 7556–7559.
- [72] J. Bang, S. Matsuishi, H. Hiraka, F. Fujisaki, T. Otomo, S. Maki, J.-I. Yamaura, R. Kumai, Y. Murakami and H. Hosono, *Journal of the American Chemical Society*, 2014, **136**, 7221–7224.
- [73] C. Tassel, Y. Goto, Y. Kuno, J. Hester, M. Green, Y. Kobayashi and H. Kageyama, *Angewandte Chemie - International Edition*, 2014, **53**, 10377–10380.
- [74] C. Tassel, Y. Goto, D. Watabe, Y. Tang, H. Lu, Y. Kuno, F. Takeiri, T. Yamamoto, C. Brown, J. Hester, Y. Kobayashi and H. Kageyama, *Angewandte Chemie - International Edition*, 2016, **55**, 9667–9670.

- [75] H. Kageyama, K. Hayashi, K. Maeda, J. Attfield, Z. Hiroi, J. Rondinelli and K. Poepfelmeier, *Nature Communications*, 2018, **9**, 1–15.
- [76] T. Yajima, F. Takeiri, K. Aidzu, H. Akamatsu, K. Fujita, W. Yoshimune, M. Ohkura, S. Lei, V. Gopalan, K. Tanaka, C. Brown, M. Green, T. Yamamoto, Y. Kobayashi and H. Kageyama, *Nature Chemistry*, 2015, **7**, 1017–1023.
- [77] R. Mikita, T. Aharen, T. Yamamoto, F. Takeiri, T. Ya, W. Yoshimune, K. Fujita, S. Yoshida, K. Tanaka, D. Batuk, A. Abakumov, C. Brown, Y. Kobayashi and H. Kageyama, *Journal of the American Chemical Society*, 2016, **138**, 3211–3217.
- [78] Y. Iwazaki, T. Suzuki, Y. Mizuno and S. Tsuneyuki, *Physical Review B - Condensed Matter and Materials Physics*, 2012, **86**, 214103–1–214103–6.
- [79] G. Bouilly, T. Yajima, T. Terashima, W. Yoshimune, K. Nakano, C. Tassel, Y. Kususe, K. Fujita, K. Tanaka, T. Yamamoto, Y. Kobayashi and H. Kageyama, *Chemistry of Materials*, 2015, **27**, 6354–6359.
- [80] T. Chatterji, T. Hansen, M. Brunelli and P. Henry, *Applied Physics Letters*, 2009, **94**, 241902–1–241902–3.
- [81] T. Chatterji, P. Henry, R. Mittal and S. Chaplot, *Physical Review B - Condensed Matter and Materials Physics*, 2008, **78**, 134105–1–134105–6.
- [82] E. Rodriguez, A. Llobet, T. Proffen, B. Melot, R. Seshadri, P. Littlewood and A. Cheetham, *Journal of Applied Physics*, 2009, **105**, 114901–1–114901–6.
- [83] M. T. Weller, *M.Sc. thesis*, New College, Oxford, 1982.
- [84] M. Weller and P. Dickens, *Solid State Ionics*, 1983, **9-10**, 1081–1085.
- [85] P. Dickens and M. Weller, *Journal of Solid State Chemistry*, 1983, **48**, 407–411.
- [86] M. Schrader, D. Mienert, T.-S. Oh, H.-I. Yoo and K. Becker, *Solid State Sciences*, 2008, **10**, 768–775.

- [87] Y. Iwazaki, T. Suzuki and S. Tsuneyuki, *Journal of Applied Physics*, 2010, **108**, 083705–1–7.
- [88] D. Crandles, B. Nicholas and C. Dreher, *Physical Review B - Condensed Matter and Materials Physics*, 1999, **59**, 12842–12846.
- [89] J. Hwang, T. Kolodiaznyi, J. Yang and M. Couillard, *Physical Review B - Condensed Matter and Materials Physics*, 2010, **82**, 214109–1–214109–8.
- [90] T. Kolodiaznyi, *Physical Review B - Condensed Matter and Materials Physics*, 2008, **78**, 045107–1–045107–5.
- [91] T. Kolodiaznyi and S. Wimbush, *Physical Review Letters*, 2006, **96**, 246404–1–246404–4.
- [92] S. Tyagi, V. Sathe, G. Sharma, V. Srihari and H. Poswal, *Journal of Materials Science*, 2018, **53**, 7224–7232.
- [93] J. Bock, S. Lee, S. Trolier-McKinstry and C. Randall, *Applied Physics Letters*, 2015, **107**, 092902–1–092902–4.
- [94] D. Tenne, X. Xi, Y. Li, L. Chen, A. Soukiassian, M. Zhu, A. James, J. Lettieri, D. Schlom, W. Tian and X. Pan, *Physical Review B - Condensed Matter and Materials Physics*, 2004, **69**, 174101–1–174101–5.
- [95] S. Kumar, D. Kumar, V. Sathe, R. Kumar and T. Sharma, *Journal of Applied Physics*, 2015, **117**, 134103–1–134103–6.
- [96] X. Liu, T. Bjørheim and R. Haugrud, *Journal of Materials Chemistry A*, 2017, **5**, 1050–1056.
- [97] V. Fritsch, J. Hemberger, M. Brando, A. Engelmayer, S. Horn, M. Klemm, G. Knebel, F. Lichtenberg, P. Mandal, F. Mayr, M. Nicklas and A. Loidl, *Physical Review B - Condensed Matter and Materials Physics*, 2001, **64**, 451131–451139.
- [98] L. Liu, H. Guo, H. Lü, S. Dai, B. Cheng and Z. Chen, *Journal of Applied Physics*, 2005, **97**, 054102–1–054102–5.

- [99] J. Marucco, M. Ocio, A. Forget and D. Colson, *Journal of Alloys and Compounds*, 1997, **262-263**, 454–458.
- [100] K. Page, T. Kolodiazhnyi, T. Proffen, A. Cheetham and R. Seshadri, *Physical Review Letters*, 2008, **101**, 205502–1–205502–4.
- [101] Y. Tang, Y. Kobayashi, K. Shitara, A. Konishi, A. Kuwabara, T. Nakashima, C. Tassel, T. Yamamoto and H. Kageyama, *Chemistry of Materials*, 2017, **29**, 8187–8194.
- [102] W. Preis and W. Sitte, *Solid State Ionics*, 2006, **177**, 3093–3098.
- [103] R. Wernicke, *Philips Research Report*, 1976, **31**, 526–543.
- [104] J. Nowotny and M. Rekas, *Ceramics International*, 1994, **20**, 265–275.
- [105] W. Preis, *Solid State Ionics*, 2017, **299**, 82–88.
- [106] J. Maier, G. Schwitzgebel and H.-J. Hagemann, *Journal of Solid State Chemistry*, 1985, **58**, 1–13.
- [107] T. Kolodiazhnyi and A. Petric, *Journal of the American Ceramic Society*, 2003, **86**, 1554–1559.
- [108] C. Bridges, F. Fernandez-Alonso, J. Goff and M. Rosseinsky, *Advanced Materials*, 2006, **18**, 3304–3308.
- [109] F. Takeiri, K. Aidzu, T. Yajima, T. Matsui, T. Yamamoto, Y. Kobayashi, J. Hester and H. Kageyama, *Inorganic Chemistry*, 2017, **56**, 13035–13040.
- [110] J. Zhang, G. Gou and B. Pan, *Journal of Physical Chemistry C*, 2014, **118**, 17254–17259.
- [111] T. Ito, A. Koda, K. Shimomura, W. Higemoto, T. Matsuzaki, Y. Kobayashi and H. Kageyama, *Physical Review B*, 2017, **95**, 020301–1–020301–5.
- [112] D. Noferini, M. Koza, P. Fouquet, G. Nilsen, M. Kemei, S. Rahman, M. Maccarini, S. Eriksson and M. Karlsson, *Journal of Physical Chemistry C*, 2016, **120**, 13963–13969.

- [113] D. Noferini, M. Koza and M. Karlsson, *Journal of Physical Chemistry C*, 2017, **121**, 7088–7093.
- [114] D. Noferini, B. Frick, M. Koza and M. Karlsson, *Journal of Materials Chemistry A*, 2018, **6**, 7538–7546.
- [115] D. Noferini, M. Koza, S. Rahman, Z. Evenson, G. Nilsen, S. Eriksson, A. Wildes and M. Karlsson, *Physical Chemistry Chemical Physics*, 2018, **20**, 13697–13704.
- [116] J. Dawson, J. Miller and I. Tanaka, *Chemistry of Materials*, 2015, **27**, 901–908.
- [117] M. Björketun, P. Sundell and G. Wahnström, *Physical Review B - Condensed Matter and Materials Physics*, 2007, **76**, 054307–1–054307–9.
- [118] Y. Jing, H. Matsumoto and N. Aluru, *Chemistry of Materials*, 2018, **30**, 138–144.
- [119] Fuel Cells Etc, *What Hydrogen Storage is Best for Me?*, <https://fuelcellsetc.com/2012/11/what-hydrogen-storage-is-best-for-me/>, accessed: 2019-02-24.
- [120] A. Züttel, *Materials Today*, 2003, **6**, 24–33.
- [121] A. Van Den Berg and C. Areán, *Chemical Communications*, 2008, 668–681.
- [122] S. McWhorter, C. Read, G. Ordaz and N. Stetson, *Current Opinion in Solid State and Materials Science*, 2011, **15**, 29–38.
- [123] T. Mandal and D. Gregory, *Annual Reports on the Progress of Chemistry - Section A*, 2009, **105**, 21–54.
- [124] N. Hanada, T. Ichikawa and H. Fujii, *Journal of Physical Chemistry B*, 2005, **109**, 7188–7194.
- [125] N. Hanada, T. Ichikawa, S. Hino and H. Fujii, *Journal of Alloys and Compounds*, 2006, **420**, 46–49.

- [126] W. Li, C. Li, H. Ma and J. Chen, *Journal of the American Chemical Society*, 2007, **129**, 6710–6711.
- [127] H. Schimmel, J. Huot, L. Chapon, F. Tichelaar and F. Mulder, *Journal of the American Chemical Society*, 2005, **127**, 14348–14354.
- [128] H. Schimmel, M. Johnson, G. Kearley, A. Ramirez-Cuesta, J. Huot and F. Mulder, *Materials Science and Engineering B: Solid-State Materials for Advanced Technology*, 2004, **108**, 38–41.
- [129] H. Schimmel, M. Johnson, G. Kearley, A. Ramirez-Cuesta, J. Huot and F. Mulder, *Journal of Alloys and Compounds*, 2005, **393**, 1–4.
- [130] P. Chen, Z. Xiong, J. Luo, J. Lin and K. L. Tan, *Nature*, 2002, **420**, 302–304.
- [131] P. Chen, Z. Xiong, J. Luo, J. Lin and K. L. Tan, *J. Phys. Chem. B*, 2003, **107**, 10967–10970.
- [132] A. Züttel, S. Rentsch, P. Fischer, P. Wenger, P. Sudan, P. Mauron and C. Emmenegger, *J. Alloys Compd.*, 2003, **356-357**, 515–520.
- [133] A. Züttel, A. Borgschulte and S. Orimo, *Scr. Mater.*, 2007, **56**, 823–828.
- [134] N. Verdál, M. Hartman, T. Jenkins, D. Devries, J. Rush and T. Udovic, *Journal of Physical Chemistry C*, 2010, **114**, 10027–10033.
- [135] N. Verdál, T. J. Udovic and J. J. Rush, *J. Phys. Chem. C*, 2012, **116**, 1614–1618.
- [136] N. Verdál, T. Udovic, J. Rush, H. Wu and A. Skripov, *Journal of Physical Chemistry C*, 2013, **117**, 12010–12018.
- [137] N. Verdál, T. J. Udovic, J. J. Rush, X. Liu, E. H. Majzoub, J. J. Vajo and A. F. Gross, *J. Phys. Chem. C*, 2013, **117**, 17983–17995.
- [138] B. Bogdanović and M. Schwickardi, *Journal of Alloys and Compounds*, 1997, **253-254**, 1–9.
- [139] B. Bogdanović, R. Brand, A. Marjanović, M. Schwickardi and J. Tölle, *Journal of Alloys and Compounds*, 2000, **302**, 36–58.

- [140] Z. Xiong, C. K. Yong, G. Wu, P. Chen, W. Shaw, A. Karkamkar, T. Autrey, M. O. Jones, S. R. Johnson, P. P. Edwards and W. I. F. David, *Nat. Mater.*, 2008, **7**, 138–141.
- [141] N. Verdal, T. J. Udovic, J. J. Rush, V. Stavila, H. Wu, W. Zhou and T. Jenkins, *J. Chem. Phys.*, 2011, **135**, 094501 1–8.
- [142] H. Wu, W. Zhou, F. E. Pinkerton, T. J. Udovic, T. Yildirim and J. J. Rush, *Energy Environ. Sci.*, 2012, **5**, 7531–7535.
- [143] I. Jain, P. Jain and A. Jain, *Journal of Alloys and Compounds*, 2010, **503**, 303–339.
- [144] E. Callini, A. Borgschulte, C. Hugelshofer, A. Ramirez-Cuesta and A. Züttel, *Journal of Physical Chemistry C*, 2014, **118**, 77–84.
- [145] G. Sandrock, K. Gross and G. Thomas, *Journal of Alloys and Compounds*, 2002, **339**, 299–308.
- [146] D. Anton, *Journal of Alloys and Compounds*, 2003, **356-357**, 400–404.
- [147] D. Pukazhselvan, B. Gupta, A. Srivastava and O. Srivastava, *Journal of Alloys and Compounds*, 2005, **403**, 312–317.
- [148] A. Zaluska, L. Zaluski and J. Ström-Olsen, *Journal of Alloys and Compounds*, 2000, **298**, 125–134.
- [149] D. Hua, Y. Hanxi, A. Xinping and C. Chuansin, *International Journal of Hydrogen Energy*, 2003, **28**, 1095–1100.
- [150] N. Verdal, T. Udovic, J. Rush and A. Skripov, *Journal of Alloys and Compounds*, 2015, **645**, S513–S517.
- [151] A. Remhof, Z. Łodziana, P. Martelli, O. Friedrichs, A. Züttel, A. Skripov, J. Embs and T. Strässle, *Physical Review B - Condensed Matter and Materials Physics*, 2010, **81**, 214304–1–214304–9.
- [152] A. Züttel, P. Wenger, S. Rentsch, P. Sudan, P. Mauron and C. Emmenegger, *Journal of Power Sources*, 2003, **118**, 1–7.

- [153] P. Martelli, A. Remhof, A. Borgschulte, R. Ackermann, T. Strässle, J. Embs, M. Ernst, M. Matsuo, S.-I. Orimo and A. Züttel, *Journal of Physical Chemistry A*, 2011, **115**, 5329–5334.
- [154] M. A. Ring and D. M. Ritter, *J. Am. Chem. Soc.*, 1961, **83**, 802–805.
- [155] E. Weiss, G. Hencken and H. Kuhr, *Chem. Ber.*, 1970, **103**, 2868–2872.
- [156] O. Mundt, G. Becker, H.-M. Hartmann and W. Z. Schwarz, *Anorg. Allg. Chem.*, 1989, **572**, 75–88.
- [157] W. Tang, M. Dimitrievska, J.-N. Chotard, W. Zhou, R. Janot, A. Skripov and T. Udovic, *Journal of Physical Chemistry C*, 2016, **120**, 21218–21227.
- [158] R. Nedumkandathil, A. Jaworski, A. Fischer, C. Österberg, Y.-C. Lin, M. Karlsson, J. Grins, A. Pell, M. Edén and U. Häussermann, *Journal of Physical Chemistry C*, 2017, **121**, 5241–5252.
- [159] H. Auer and H. Kohlmann, *Zeitschrift für Anorganische und Allgemeine Chemie*, 2017, **643**, 945–951.
- [160] R. Janot, W. Tang, D. Cléménçon and J.-N. Chotard, *Journal of Materials Chemistry A*, 2016, **4**, 19045–19052.
- [161] J. Mink, Y.-C. Lin, M. Karlsson, C. Österberg, T. Udovic, H. Fahlquist and U. Häussermann, *Journal of Raman Spectroscopy*, 2017, **48**, 284–291.
- [162] K. Lefmann, *Neutron Scattering: Theory, Instrumentation, and Simulation*, 2007, https://www.fys.ku.dk/~willend/Neutron1_4.pdf.
- [163] M. Jiang, *Neutron Scattering for Experimental Research*, 2013, <http://large.stanford.edu/courses/2013/ph241/jiang2/>.
- [164] A. Munter (NCNR), *Neutron scattering lengths and cross sections*, <https://www.ncnr.nist.gov/resources/n-lengths/>, accessed: 2019-02-24.
- [165] T. Brückel, J. Voigt, G. Heger, G. Roth, H. Frielinghaus, J. Stellbrink, R. P. Hermann, E. Kentzinger, U. Rücker, R. Zorn, M. Angst and D. Richter, *Neutron scattering*, Forschungszentrum Jülich GmbH, 2014, vol. 84.

- [166] *Neutron Applications in Earth, Energy and Environmental Sciences*, ed. L. Liang, R. Rinaldi and H. Schober, Springer: New York, 2009.
- [167] E. Suard, G. Julio and C. Ritter, *D2B - High-resolution two-axis diffractometer*, <https://www.ill.eu/users/instruments/instruments-list/d2b/characteristics/>, accessed 2019-02-24.
- [168] L. E. Smart and E. A. Moore, *Solid State Chemistry: An Introduction*, Taylor & Francis: Boca Raton, Third Edition edn., 2005.
- [169] D. Marquardt, R. J. Alsop, M. C. Rheinstädter and T. A. Harroun, *Journal of Cardiovascular Development and Disease*, 2015, **2**, 125–140.
- [170] T. Ramirez-Cuesta, P. Stewart and J. Tomkinson, *TOSCA User Manual*, <https://www.isis.stfc.ac.uk/Pages/tosca-user-manual6685.pdf>, accessed 2019-02-20.
- [171] K. J. Alvine, M. Tyagi, C. M. Brown, T. J. Udovic, T. Jenkins and S. G. Pitman, *J. Appl. Phys.*, 2012, **111**, 053505–1 – 053505–7.
- [172] P. C. H. Mitchell, S. F. Parker, A. Ramirez-Cuesta, and J. Tomkinson, *Vibrational Spectroscopy with Neutrons*, Word Scientific, Singapore, 2005.
- [173] V. F. Sears, *Neutron News*, 1992, **3**, 26–37.
- [174] S. F. Parker, S. M. Bennington, A. J. Ramirez-Cuesta, G. Auffermann, W. Bronger, H. Herman, K. P. J. Williams and T. Smith, *Journal of the American Chemical Society*, 2003, **125**, 11656–11661.
- [175] J. Tomkinson, S. Parker and D. Lennon, *Journal of Chemical Physics*, 2010, **133**, 034508–8.
- [176] L. Mazzei, A. Perrichon, A. Mancini, G. Wahnström, L. Malavasi, S. F. Parker, L. Börjesson and M. Karlsson, *J. Mater. Chem. A*, 2019, DOI: 10.1039/C8TA06202A.
- [177] M. Bée, *Quasielastic Neutron Scattering*, IOP Publishing, Bristol, D.J. Millen ed., 1988.

- [178] R. Hempelmann, *Quasielastic neutron scattering and solid state diffusion*, Clarendon Press, Oxford, 2000.
- [179] T. Yildirim, P. M. Gehring, D. A. Neumann, P. E. Eaton and T. Emrick, *Phys. Rev. B*, 1999, **60**, 314–321.
- [180] A. Remhof, P. Mauron, A. Züttel, J. P. Embs, Z. Łodziana, A. J. Ramirez-Cuesta, P. Ngene and P. de Jongh, *J. Phys. Chem. C*, 2013, **117**, 3789–3798.
- [181] *Neutron Spin Echo Spectroscopy*, ed. F. Mezei, C. Pappas and T. Gutberlet, Springer Berlin Heidelberg, Berlin, Heidelberg, 2003, vol. 601.
- [182] J. Stewart, P. Deen, K. Andersen, H. Schober, J.-F. Barthélémy, J. Hillier, A. Murani, T. Hayes and B. Lindenau, *Journal of Applied Crystallography*, 2009, **42**, 69–84.
- [183] B. Farago, in *Neutron Data Booklet*, ed. A.-J. Dianoux and G. Lander, OCP Science, Philadelphia, Second edition edn., 2003, ch. The basics of neutron spin echo.
- [184] P. Stewart and R. Svemir, *TOSCA: A World Class Inelastic Neutron Spectrometer*, <http://www.isis.stfc.ac.uk/instruments/tosca/4715.html>, accessed 2019-02-24.
- [185] S. F. Parker, F. Fernandez-Alonso, A. J. Ramirez-Cuesta, J. Tomkinson, S. Rudic, R. S. Pinna, G. Gorini and J. F. Castañón, *Journal of Physics: Conference Series*, 2014, **554**, 012003.
- [186] A. Devashibhai and H. Walker, *MERLIN*, <https://www.isis.stfc.ac.uk/Pages/Merlin.aspx>, accessed: 2019-02-24.
- [187] R. Bewley, R. Eccleston, K. McEwen, S. Hayden, M. Dove, S. M. Bennington, J. Treadgold and R. Coleman, *Phys. B Condens. Matter*, 2006, **385-386**, 1029–1031.
- [188] P. C. H. Mitchell, S. F. Parker, A. J. Ramirez-Cuesta and J. Tomkinson, *Vibrational Spectroscopy with Neutrons*, World Scientific: Singapore, 2005, vol. 3.

- [189] Y. Cheng, L. Daemen, A. Ramirez-Cuesta, L. Jones and R. Goyette, *Vibrational Spectrometer VISION*, <https://neutrons.ornl.gov/vision>, accessed: 2019-02-24.
- [190] J. R. D. Copley and J. C. Cook, *Chem. Phys.*, 2003, **292**, 477–485.
- [191] N. Butch, W. Zhou and C. Brown, *DCS Disk Chopper Spectrometer*, <http://ncnr.nist.gov/instruments/dcs/>, accessed: 2019-02-24.
- [192] M. Tyagi and T. Prisk, *High Flux Backscattering Spectrometer*, <http://ncnr.nist.gov/instruments/hfbs/>, accessed 2019-02-24.
- [193] A. Meyer, R. M. Dimeo, P. M. Gehring and D. A. Neumann, *Review of Scientific Instruments*, 2003, **74**, 2759–2777.
- [194] B. Frick, E. Mamontov, L. Van Eijck and T. Seydel, *Zeitschrift fur Physikalische Chemie*, 2010, **224**, 33–60.
- [195] B. Frick, T. Seydel and M. Appel, *IN16B*, <https://www.ill.eu/users/instruments/instruments-list/in16b/description/instrument-layout/>, accessed: 2019-02-24.
- [196] E. Mamontov and K. Herwig, *Review of Scientific Instruments*, 2011, **82**, 085109–1–085109–10.
- [197] N. Rosov, S. Rathgeber and M. Monkenbusch, *Scattering from polymers: characterization by x-rays, neutrons, and light*, Washington DC, 2000, pp. 103–116.
- [198] A. Faraone and M. Nagao, *CHRNS NSE - Neutron Spin Echo Spectrometer*, <https://www.ncnr.nist.gov/instruments/nse/>, accessed: 2019-02-24.
- [199] T. C. Hansen, P. F. Henry, H. E. Fischer, J. Torregrossa and P. Convert, *Measurement Science and Technology*, 2008, **19**, 034001.
- [200] T. C. Hansen, C. Ritter and S. Savvin, *D20*, <https://www.ill.eu/users/instruments/instruments-list/d20/description/instrument-layout/>, accessed: 2019-02-24.

- [201] C. Österberg, H. Fahlquist, U. Häussermann, C. M. Brown, T. J. Udovic and M. Karlsson, *The Journal of Physical Chemistry C*, 2016, **120**, 6369–6376.
- [202] M. Dimitrievska, J.-N. Chotard, R. Janot, A. Faraone, W. Tang, A. Skripov and T. Udovic, *Journal of Physical Chemistry C*, 2018, **122**, 23985–23997.
- [203] F. Denis Romero, A. Leach, J. Möller, F. Foronda, S. Blundell and M. Hayward, *Angewandte Chemie - International Edition*, 2014, **53**, 7556–7559.
- [204] Y. Peltzer, *International Journal of Hydrogen Energy*, 2016, **41**, 5682–5687.
- [205] M. Santhosh, S. Kanagaprabha, R. Rajeswarapalanichamy, G. Sudha Priyanga and K. Iyakutti, *Journal of Physics and Chemistry of Solids*, 2015, **81**, 34–39.
- [206] P. Vajeeston, P. Ravindran and H. Fjellvåg, *Inorganic Chemistry*, 2008, **47**, 508–514.
- [207] P. Vajeeston, P. Ravindran, A. Kjekshus and H. Fjellvåg, *Journal of Alloys and Compounds*, 2008, **450**, 327–337.
- [208] E. Mamontov, A. Kolesnikov, S. Sampath and J. Yarger, *Scientific Reports*, 2017, **7**, 1–7.
- [209] Y. Song, *Physical Chemistry Chemical Physics*, 2013, **15**, 14524–14547.
- [210] *ESS European Spallation Source*, <https://europeanspallationsource.se/>, accessed 2019-02-08.
- [211] S. W. Lovesey, *Theory of neutron scattering from condensed matter.*, Clarendon, Oxford, 1984.
- [212] G. L. Squires, *Introduction to the Theory of Thermal Neutron Scattering.*, Cambridge University Press, Cambridge, 2012.

- [213] C. Pappas, G. Ehlers and F. Mezei, in *Neutron Scattering from Magnetic Materials*, ed. T. Chatterji, Elsevier Science, Amsterdam, 2006, pp. 521 – 542.
- [214] M. H. Levitt, *Spin dynamics: Basics of nuclear magnetic resonance.*, John Wiley and Sons, Hoboken, NJ, 2007.